Supplementary Materials for

Oxygen-Bridged Dual Catalytic Sites Enable Asymmetric C-C Coupling for Efficient CO_2 Electroreduction to Ethanol

Shifu Wang[1,2,‡], Jian Zhao[3,‡], Ouardia Akdim[4], Yaqiong Zeng[1], Xiyu Li[1], Weijue Wang[1], Ying-Rui Lu[5], Wei Xu[6,7], Xuning Li[1,*], Yanqiang Huang[1,2,*], Graham J. Hutchings[4,*], Bin Liu[8,9,*] and Tao Zhang[1]

[1]State Key Laboratory of Catalysis, Dalian Institute of Chemical Physics, Chinese Academy of Sciences, Dalian 116023, P. R. China

[2]Department of Chemical Physics, University of Science and Technology of China, Hefei 230026, P. R. China

[3]School of Chemistry and Chemical Engineering, Liaoning Normal University, Dalian 116029, P. R. China

[4]Max Planck-Cardiff Centre on the Fundamentals of Heterogeneous Catalysis FUNCAT, Cardiff Catalysis Institute, School of Chemistry, Cardiff University, Cardiff, United Kingdom

[5]National Synchrotron Radiation Research Center, Hsinchu 300, Taiwan

[6]Beijing Synchrotron Radiation Facility, Institute of High Energy Physics, Beijing 100049, P. R. China

[7]RICMASS, Rome International Center for Materials Science Superstripes, Via dei Sabelli 119A, Roma 00185, Italy

[8] Department of Materials Science and Engineering, City University of Hong Kong, Hong Kong SAR 999077, P. R. China

[9]Department of Chemistry, Hong Kong Institute for Clean Energy (HKICE) & Center of

Super-Diamond and Advanced Films (COSDAF), City University of Hong Kong, Hong Kong SAR 999077, P. R. China

‡These authors contributed equally to this work

*Corresponding authors: lixn@dicp.ac.cn (X.L.), yqhuang@dicp.ac.cn (Y.H.), hutch@cardiff.ac.uk (G.H.) and bliu48@cityu.edu.hk (B.L.)

Methods

Chemicals and materials

Copper (II) chloride dihydrate ($CuCl_2 \cdot 2H_2O$), glucose ($C_6H_{12}O_6$), hexadecylamine (HDA), triethylamine were purchased from Aladdin. Isopropyl alcohol (C_3H_8O), potassium bicarbonate ($KHCO_3$, 99.9%), potassium hydroxide (KOH, 99.9%) were purchased from Sigma-Aldrich. Nafion 117 solution (5 wt.%) was purchased from Alfa Aesar. Carbon paper (YSL-30T) was purchased from FuelCell Store. All chemical reagents were used as received without any further purification. Deionized water (18.2 MΩ) was used in all experimental processes.

Preparation of Cu nanowires

Uniform copper nanowires (Cu NW) were synthesized following a previously reported method with slight improvements[1]. In a typical synthesis, glucose (250 mg, 1.4 mmol), $CuCl_2 \cdot 2H_2O$ (117 mg, 0.7 mmol), and hexadecylamine (900 mg, 3.8 mmol) were dissolved in 50 mL of deionized water under vigorous stirring at 50 ℃ for 12 hours. Subsequently, the homogeneous solution was kept in a water bath at 75 ℃ and stirred for 24 hours until it turned brown. The solution was then transferred to a 150 mL pressure bottle and heated at 120 ℃ for 24 hours. After cooling to room temperature, the products were collected by centrifugation at 12,000 rpm for 5 minutes. The obtained reddish-brown Cu NW was washed several times with hot deionized water (60 ℃), ethanol, and hexane to remove excess hexadecylamine and glucose, and dried under vacuum at 60 ℃ for 12 hours.

Preparation of hydroxylated Cu nanowires

Hydroxylated Cu nanowires (O-Cu NW) were synthesized using an alkali etching strategy. Specifically, 100 mg of Cu NW were uniformly dispersed in a 1 M KOH solution. After 30 minutes of ultrasonic treatment, the alkali-treated copper nanowires were immediately filtered and washed

three times with water and then with ethanol. The washed nanowires were transferred to a vacuum oven and dried at 60 ℃.

Preparation of chlorophthalocyanine iron

Chlorophthalocyanine iron (Cl-FePc) was synthesized using a standard method based on previously published procedures. In a 25 mL round-bottom flask, 3 g of phthalonitrile, 0.9519 g of anhydrous ferric chloride ($FeCl_3$), and 6 mL of chloronaphthalene were combined. The mixture was heated to 180 ℃ and refluxed for 24 hours. The product was then filtered, washed with acetone, and dried overnight under vacuum at 60 ℃, resulting in a dark green solid.

Preparation of oxygen-bridged FeN_4-O-Cu NW

For the synthesis of the oxygen-bridged FeN_4-O-Cu NW catalyst, 5 mg of Cl-FePc and 100 mg of hydroxylated Cu nanowires were dispersed in 50 mL of ethanol by sonication for 30 minutes. Then, 1 mL of trimethylamine was added. The dispersion was stirred and refluxed at 95 ℃ for 24 hours. The product was filtered, washed with ethanol and water, and vacuum-dried sequentially. The preparation of ^{57}Fe-enriched $^{57}FeN_4$-O-Cu NW followed the same procedure as that of FeN_4-O-Cu NW, except that $^{57}FeCl_3$ was prepared by dissolving ^{57}Fe foil in an HCl solution followed by H_2O_2 oxidation.

Electrochemical Measurements

Electrochemical measurements were performed at room temperature and ambient pressure on a glassy carbon electrode in a two-compartment H-cell filled with CO_2-saturated 0.1 M potassium bicarbonate ($KHCO_3$) electrolyte using an electrochemical workstation. A three-electrode cell configuration was employed, with a glassy carbon rotating disc electrode (RDE, diameter 2 mm) as the working electrode, a platinum foil (1.5×1.5 cm^2) as the counter electrode, and a saturated calomel

electrode (SCE, Hg/Hg_2Cl_2) as the reference electrode. To prepare the catalyst ink, 5 mg of catalyst and 40 μL of 5 wt.% Nafion solution were introduced into a water and isopropyl alcohol solution (960 μL, 1:1 v/v) and ultrasonicated for 3 hours. The catalyst ink (20 μL) was then applied onto a glassy carbon RDE and allowed to dry in air, resulting in a catalyst loading of 0.5 mg cm^{-2}. Cyclic voltammetry (CV) and linear sweep voltammetry (LSV) were conducted in CO_2-saturated 0.1 M $KHCO_3$ solution on an RDE at a rotating speed of 1600 rpm with a scan rate of 5 mV s^{-1}. All potentials were calculated with respect to the reversible hydrogen electrode (RHE) scale according to the Nernst equation: $\mathrm{E\,(vs.\,RHE)} = \mathrm{E\,(vs.\,SCE)} + 0.2415 + 0.0591 \times \mathrm{pH}$

Carbon paper (AVCarb P75, FuelCellStore) was repeatedly soaked in a polytetrafluoroethylene (PTFE) solution until the weight of PTFE reached 25 wt.%. The carbon paper was heated in air at 350 ^{o}C for 2 h. A carbon black (Vulcan XC-72R, Sigma) ink containing 40 wt.% PTFE was drop-casted on one side of the above carbon paper. After further heating in air at 350 ^{o}C for 2 h, the GDL was prepared. The catalyst (4 mg) and Nafion solution (~5 wt.% in a mixture of isopropyl alcohol and water, DuPont) were firstly mixed and dispersed into isopropyl alcohol under ultrasonication for 30 min to form a uniform catalyst ink. Then, the catalyst ink (1 mL) was spray-casted onto a GDL (2 × 2 cm^2), affording a catalyst loading of 1 mg cm^{-2}, and dried at 60 ℃ to form the GDE.

The electrochemical measurements were also performed in a flow cell separated by an anion exchange membrane using a CHI660e electrochemical workstation at room temperature. The flow cell was equipped with three electrodes, in which the Ag/AgCl electrode as the reference electrode and Ni-foam as the counter electrode. The gas diffusion electrode (GDE) was prepared by spraying the catalyst ink onto one side of the carbon paper (2 cm × 2 cm) to realize a mass loading of 1 mg

cm^{-2}. CV and LSV curves were recorded on a CHI660E electrochemical workstation in 1 M KOH (pH = 14) at a scan rate of 5 mV s^{-1} from −1.0 to −2.5 V vs. SHE. All potentials were converted to the reversible hydrogen electrode (RHE) scale by the following equation: $\mathrm{E\ (vs.\,RHE)} = \mathrm{E\ (vs.\,Ag/AgCl)} + 0.197\ \mathrm{V} + 0.0591 \times \mathrm{pH}$

Faradaic efficiency evaluation

The products of electrochemical CO_2 reduction reaction (CO_2RR) were measured using chronoamperometry at each fixed potential in a CO_2RR electrolysis cell. The electrolyte in the cathodic compartment was stirred at a rate of 500 rpm during electrolysis. CO_2 gas was introduced into the cathodic compartment at a rate of 20 sccm and was routed into a gas chromatograph (GC, Agilent 8860). The gas chromatograph was equipped with a Molecular Sieve 5A capillary column and a packed Carboxen-1000 column. The gaseous products (H_2, CO, CH_4, and C_2H_4) were quantified by gas chromatograph equipped with a flame ionization detector (FID) for CO, CH_4 and C_2H_4, and a thermal conductivity detector (TCD) for H_2. Ultrapure nitrogen (N_2, 99.9999%) was used as the carrier gas. The liquid products (HCOOH and CH_3CH_2OH) were examined by nuclear magnetic resonance spectroscopy (NMR). ^{1}H NMR spectra were collected on a Bruker Avance III HD 400 NMR spectroscope in 10% D_2O using water suppression mode, with DMSO as an internal standard. All Faradaic efficiencies and error bars reported in this work were determined from the average of at least three replicates for each potential studied.

Characterization

The crystal structure of Cu NW, O-Cu NW and FeN_4-O-Cu NW were characterized by X-ray diffraction (XRD, Bruker AXS D8 Advance) with Cu K_α radiation (λ = 1.5406 Å). The morphology of the catalysts was examined by transmission electron microscopy (HRTEM, JEOL JEM-2100F

operated at 200 kV) and field-emission scanning electron microscopy (FESEM, JSM-6700F) equipped with an energy dispersive X-ray spectroscopy (EDX, Aztec X-Max 80T). High-angle annular dark-field scanning transmission electron microscopy (HAADF-STEM) characterization was conducted on a JEOL JEMARM200F STEM/TEM with a guaranteed resolution of 0.08 nm. Detailed chemical compositions were analyzed by X-ray photoelectron spectroscopy (XPS) on an ESCALAB 250 photoelectron spectrometer (Thermo Fisher Scientific) using a monochromatic Al K_α X-ray beam (1,486.6 eV). All binding energies were referenced to the C1s peak (284.8 eV). The concentration of Fe in FeN_4-O-Cu NW and FeN_4-Cu NW were quantified by inductively coupled plasma optical emission spectroscopy (ICP-OES). The room temperature ^{57}Fe Mössbauer spectra of the samples were measured using a WisseEI E spectrometer with a MR-360 drive unit and ^{57}Co:Rh source. For *ex-situ* XAS, a certain amount of powder samples were placed into a hollow circular mold (made of polytetrafluoroethylene) with a diameter of 1 cm. The filled sample was then fixed and vacuumed to prevent oxidation during the transfer and measurement processes. Finally, the sample was secured on an XAS sample stage, which was positioned at a 45 ° angle to the X-ray during the measurement, allowing for collection of fluorescence signals.

***Operando* Mössbauer measurements**

^{57}Fe Mössbauer spectra were recorded on a WSS-10 spectrometer control by Wissoft 2003; JANIS Cryostat SHI-850-5 used for temperature control at 6 K in constant acceleration mode. ^{57}Co (Rh) was used as the radiation source. MossWinn 4.0 has been used for the quantitative evaluation of the spectral parameters (least-squares fitting to Lorentzian peaks). The minimum experimental line widths were 0.27 mm s^{-1}. The temperature of the samples was controlled by a LakeShore Modle 335 within an accuracy of ±0.3 K. Isomer shifts were determined relative to α-iron at 298 K.

Operando XAS measurements

X-ray Absorption Spectroscopy (XAS) and operando XAS measurements were performed in the total-fluorescence yield (TFY) mode at room temperature. These measurements utilized the TPS 32A and TLS01C1 beamlines at the National Synchrotron Radiation Research Center (NSRRC) in Taiwan. Energy calibration was performed with a Cu and Fe foil standard by shifting all spectra to a glitch in the incident intensity. Fluorescence spectra were recorded using a silicon drift detector. The measurement in a typical three-electrode setup, the same condition as that in electrochemical characterization was performed in a specially designed Teflon container with a window sealed by Kapton tape[1-3]. CO_2RR was conducted on a Bio-logic VSP potentiostat in a standard three-electrode setup. The spectral time recording was 40 min for a single spectrum (2 s for the pre-edge region, 2 s for the rising-edge region, and 8 s for the EXAFS region) during CO_2RR. The pre-edge baseline was subtracted, and the spectrum was normalized to the post-edge. EXAFS analysis was conducted using a Fourier transform on k2-weighted EXAFS oscillations to evaluate the contribution of each bond pair to the Fourier transform peak.

Operando ATR-SEIRAS measurements

The *operando* attenuated total reflectance surface enhanced infrared absorption spectroscopy (ATR-SEIRAS) measurements were performed on a Nicolet iS20 FTIR spectrometer equipped with a MCT detector cooled using liquid nitrogen and PIKE VeeMAX III variable angle ATR sampling accessory. The catalyst was added dropwisely to the surface of Au-plated silicon as the working electrode. A graphite rod and an Ag/AgCl electrode were used as the counter and reference electrode in all tests, respectively. The background was taken at OCV in CO_2-saturated 0.1 M $KHCO_3$ electrolyte. Afterwards, potential-dependent spectra were collected during stepping the working

electrode potential from -0.4 to -1.6 V (*vs.* RHE). The step width and duration are 0.1 V and 120 s, respectively.

Computational details

The CO_2 reduction reaction for Cu(111)-OFePc was studied via density functional theory (DFT), in which all calculations were performed via OpenMX 3.9.9[4,5]. A fully relativistic DFT implementation with localized pseudoatomic orbitals[6,7] and norm-conserving pseudopotentials[8] was used for all above calculations. The exchange-correlation interaction was calculated by the generalized gradient approximation (GGA) method with the Perdew−Burke−Ernzerhof (PBE)[9,10] pure functional. The basis functions were taken as C6.0-s2p2d1, H6.0-s2p1, N6.0-s2p2d1, O6.0-s2p2d1, and Fe6.0S-s3p2d1 (the pseudopotential cutoff radius is followed by a basis set specification). The long-range van der Waals (vdW) interactions were considered by Grimme's DFT-D3 scheme[11]. The accuracy of the real-space numerical integration was specified by the cutoff energy of 300 Ry; the total energy convergence criterion was 1×10^{-6} eV. The k-mesh for Brillouin zones of 7×7 supercells was specified as $1\times1\times1$ mesh for Cu(111). The vacuum layer was set to 15 Å avoiding the interaction among mirror images[12]. As for the structure optimization, all atoms were allowed to fully relax with the conjugate gradient method until the maximum force on any atom was smaller than 0.05 eV $Å^{-1}$.

For the electrocatalytic CO_2RR process, the model of the computational hydrogen electrode (CHE)[13] was used to calculate the energy of a proton–electron pair, where the energy of a proton-electron pair was approximated as one-half of the free energy of H_2 molecule under standard conditions[14,15]. The Gibbs free energy (ΔG) for each electrochemical process was performed by ALAMODE code on the condition of 298 K and 1 atm.

The linear relationship between electron density and IS

The Mössbauer parameters were computed using the ORCA software, employing the B3LYP functional and def2-TZVP basis set, consistent with the optimization protocol. The isomer shift (δ), also referred to as the chemical shift, is predominantly determined by the electron density at the iron nucleus. It is expressed by the following equation:

$$\delta = \alpha(\rho_s - \rho_r) \quad (1)$$

where: ρ_s is the electron density at the nucleus in the sample, ρ_r is the electron density at the nucleus in the reference compound, α is a calibration constant that depends on the specific Mössbauer isotope (for ^{57}Fe, α ≈ -0.29 mm/s au^{-3}).

In practical applications, the equation can be reformulated as:

$$\delta_i = k\rho_i(0) + b \quad (2)$$

This linear relationship is established by fitting a series of reference compounds, enabling the determination of the isomer shift (IS) for the target compound. It is important to note that ρ, as well as the coefficients k and b, are influenced by the theoretical approach (e.g., DFT approximation level, basis set).

In this study, thirteen distinct iron complexes were utilized to derive the coefficients k and b, resulting in the following linear equation for the IS of Fe:.

$$IS = -0.2786\rho + 3227.0 \ (R^2 = 0.9121) \quad (3)$$

Based on the equation (3) and the linear relationship between IS and electron density IS = -0.2786ρ + 3277, we have performed calculations on FeN_4-O-Cu NW to gain QS and IS values as listed in Supplementary Table 5, where the QS values are 2.27 mm s^{-1}, the ρ(Fe) values are 11761.055 a.u.^{3}, thus the IS values are 0.37 mm s^{-1}, respectively. It can be seen that the calculated IS values are close

to the experimental results.

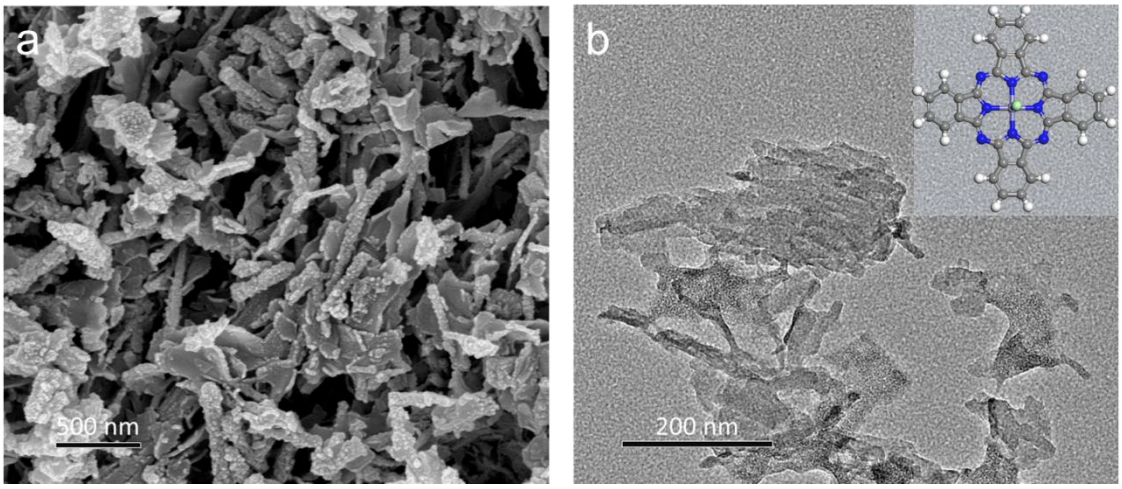

Supplementary Fig. 1 | a, SEM and b, TEM images of iron chlorophthalocyanine (Cl-FePc). (The inset in Supplementary Fig. 2b shows the model structure of the Cl-FePc molecule).

As shown in Supplementary Fig. 1, SEM and TEM results demonstrate that iron chlorophthalocyanine (Cl-FePc) molecules exhibit a uniform two-dimensional sheet-like structure.

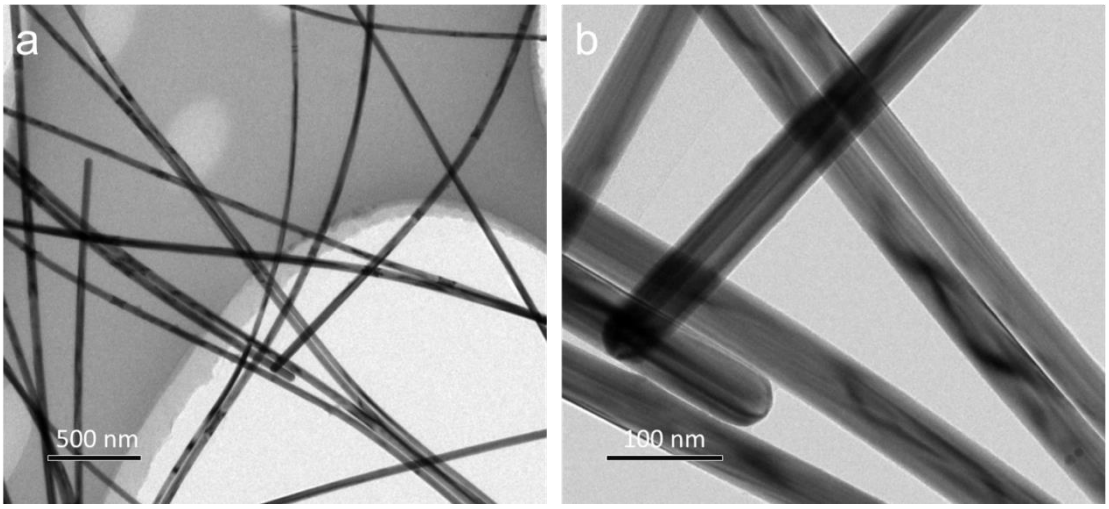

Supplementary Fig. 2 | TEM images of copper nanowires (Cu NW) at different magnifications.

As shown in Supplementary Fig. 2, uniformly distributed copper nanowires (Cu NW) were successfully synthesized, with transmission electron microscopy (TEM) images displaying one-dimensional copper nanowires with a high aspect ratio and a diameter of approximately 45 ± 3 nm.

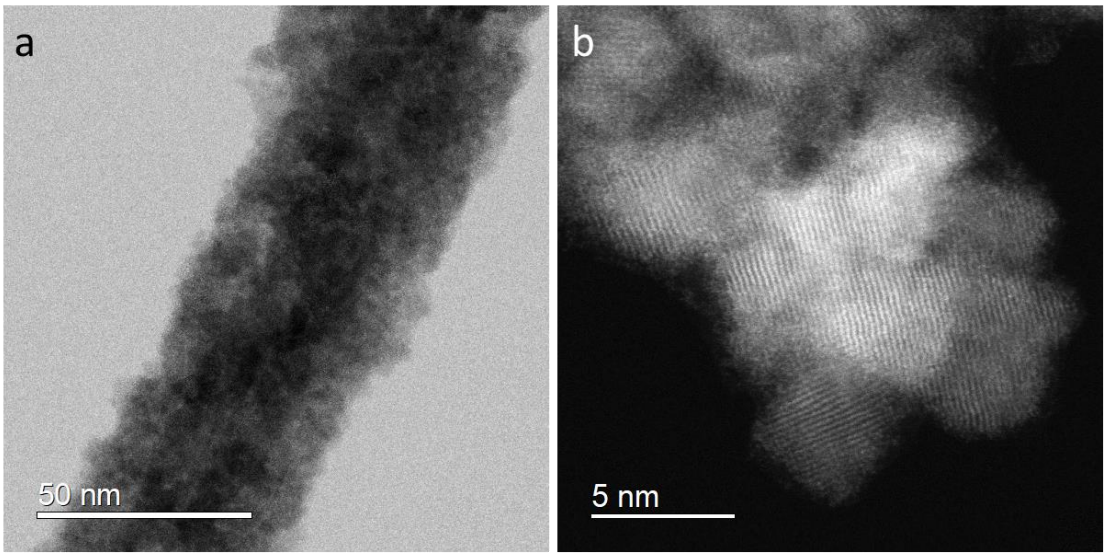

Supplementary Fig. 3 | a, b, TEM (scale bars: 50 nm) and HAADF-STEM (scale bars: 5 nm) images of FeN_4-O-Cu NW.

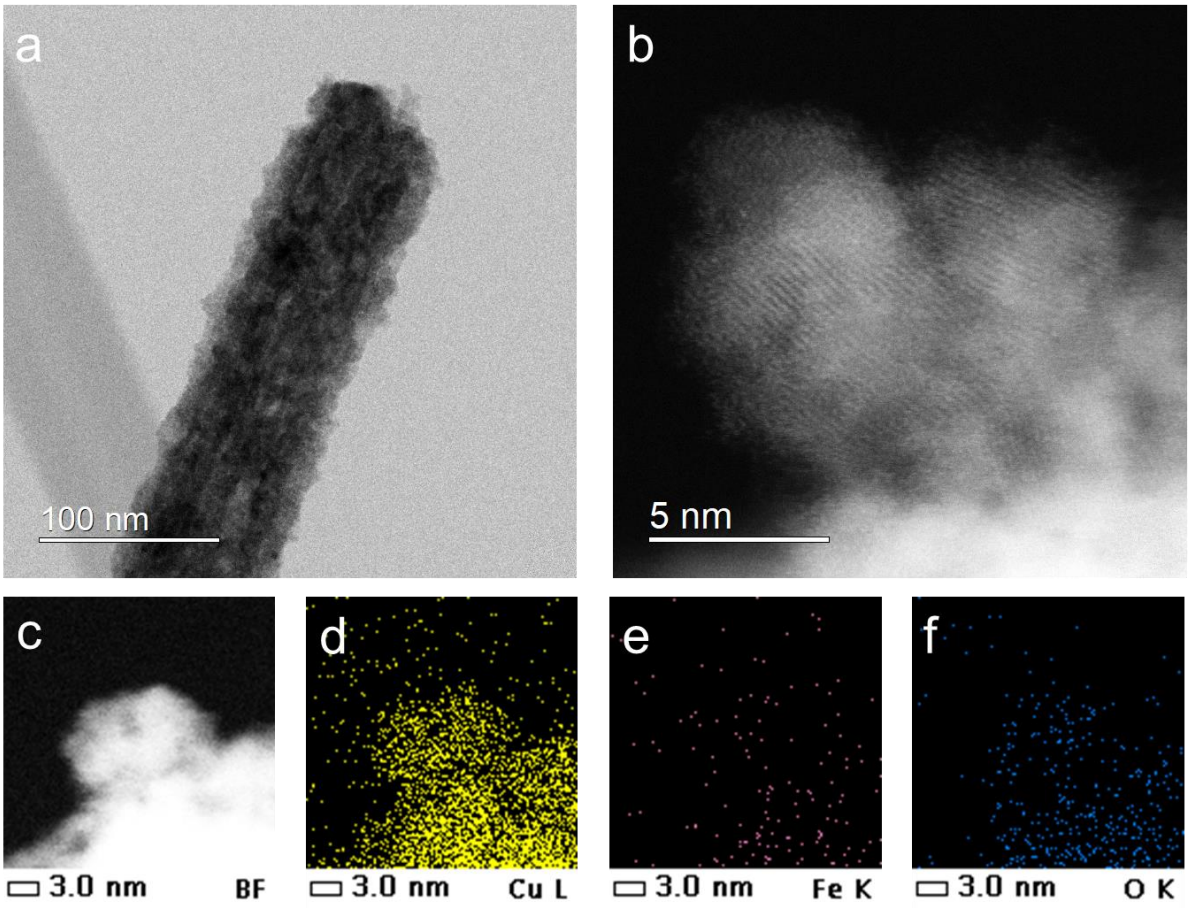

Supplementary Fig. 4 | a, b, TEM (scale bars: 100 nm) and HAADF-STEM (scale bars: 5 nm) images of FeN_4-O-Cu NW. c-f, The EDX elemental mapping images of FeN_4-O-Cu NW (scale bars: 3 nm).

One-dimensional FeN_4-O-Cu NW catalysts, with an average diameter of 50 ± 5 nm, were imaged using transmission electron microscopy (TEM) (see Supplementary Fig. 4). High-magnification high-angle annular dark-field scanning transmission electron microscopy (HAADF-STEM) and energy-dispersive X-ray spectroscopy (EDX) mapping images of FeN_4-O-Cu NW reveal the absence of Fe clusters or nanoparticles, showing that isolated Fe atoms are uniformly distributed across the surface of the hydroxylated-Cu nanowire matrix in FeN_4-O-Cu NW.

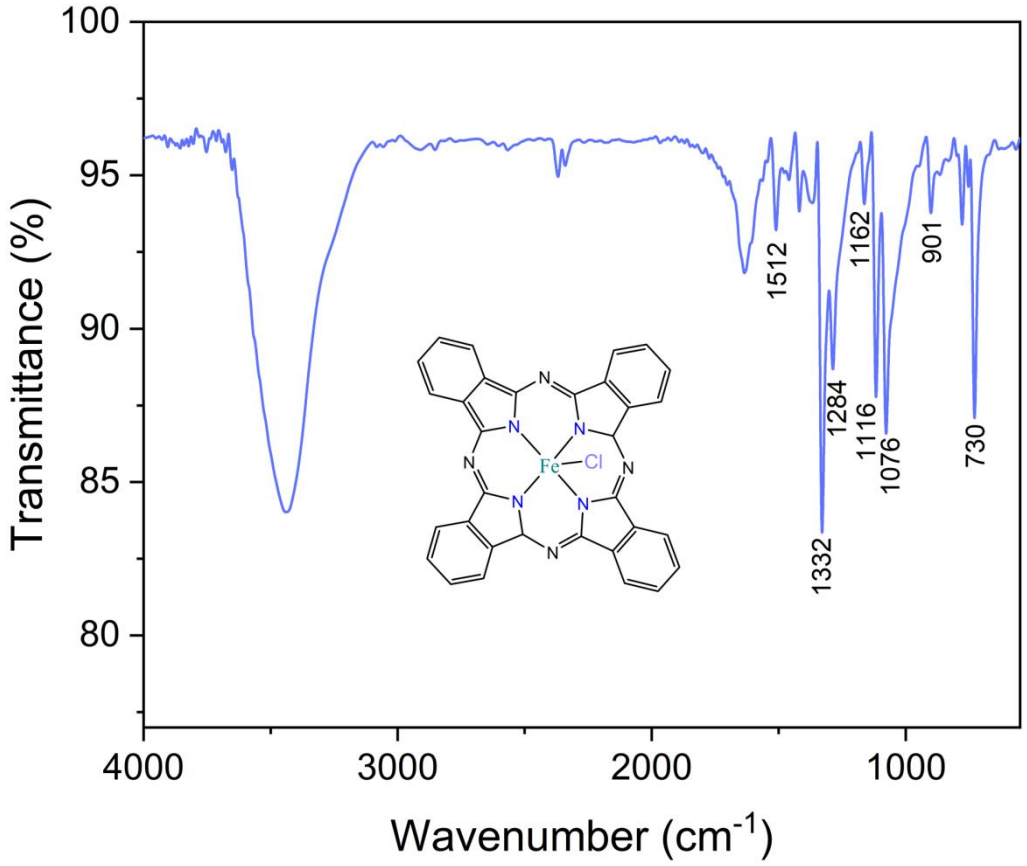

Supplementary Fig. 5 | Fourier transform infrared spectroscopy (FT-IR) spectrum of the as-synthesized Cl-FePc molecule.

The main peaks at 730, 1076, and 1116 cm^{-1} can be attributed to the out-of-plane and in-plane C-H bond vibrations from the Pc ring, respectively, while the bands at 1162 and 1332 cm^{-1} correspond to the C-N and C-C stretching vibrations from the isoindole structure.

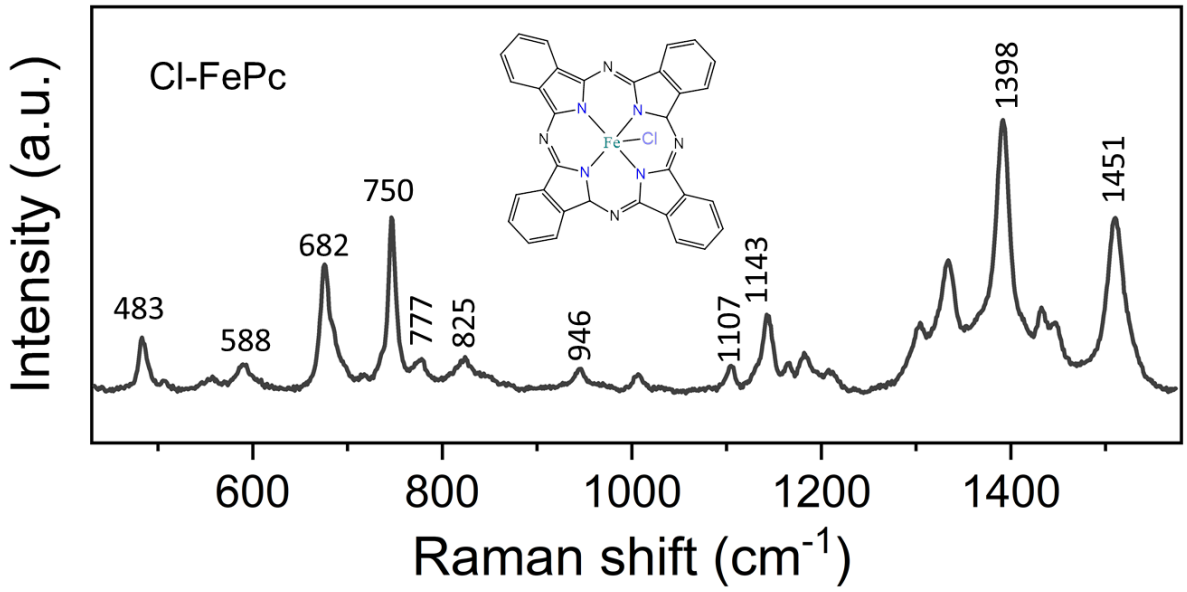

Supplementary Fig. 6 | Raman spectrum of the as-synthesized Cl-FePc molecule.

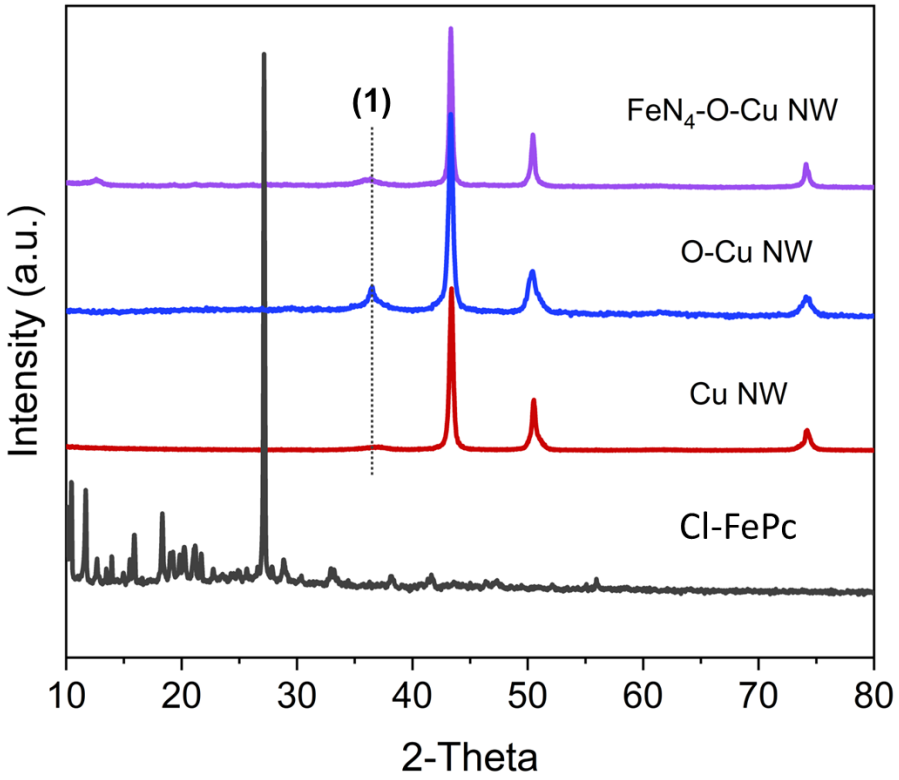

Supplementary Fig. 7 | XRD patterns of Cl-FePc, Cu NW, O-Cu NW, and FeN_4-O-Cu NW.

The XRD pattern of the as-prepared Cu NW shows three peaks at 43.4 °, 50.5 °, and 74.2 °, corresponding to the diffraction from Cu(111), (200), and (220) planes. And the broad XRD diffraction peak located at 36.5 ° (position (1)) could be attributed to the amorphous Cu_xO phase, which is related to the hydroxylation treatment of the copper surface. Except for the broad peak at 36.5 ° related to the surface oxidation of copper, the characteristics of the XRD diffraction peaks are similar to those of Cu NW and O-Cu NW, suggesting atomic dispersion of Fe species in FeN_4-O-Cu NW. Also, no XRD diffraction peaks related to Cl-FePc were observed.

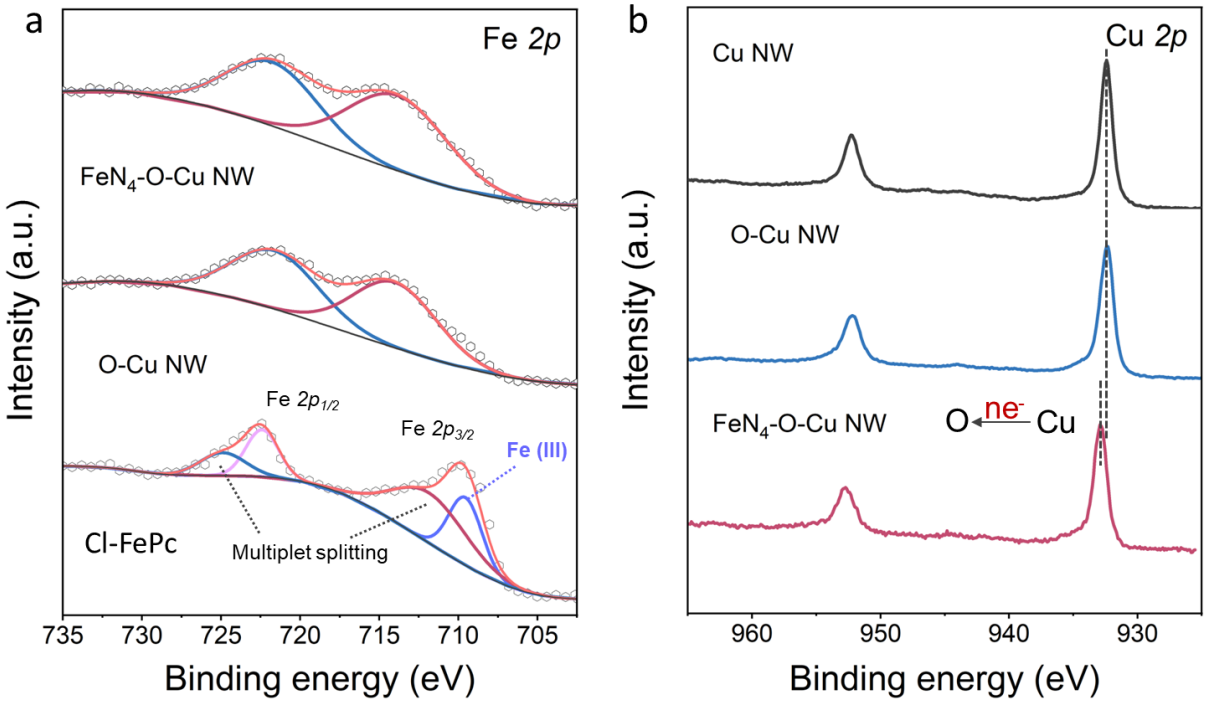

Supplementary Fig. 8 | a, b, High-resolution Fe 2*p* and Cu *2p* XPS spectra of Cu NW, O-Cu NW, Cl-FePc and FeN_4-O-Cu NW.

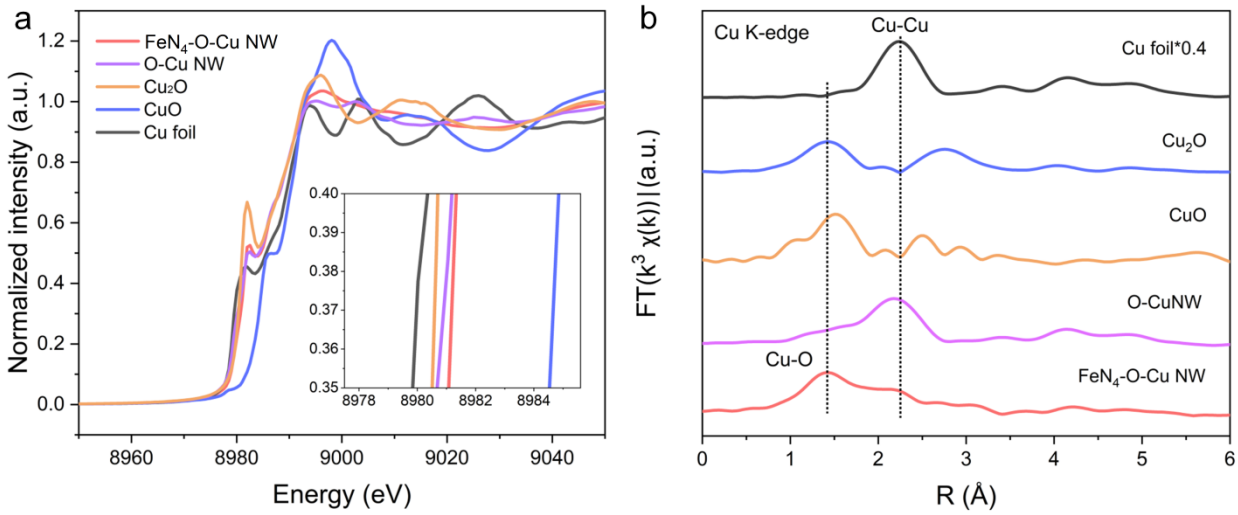

Supplementary Fig. 9 | a, Normalized Cu K-edge XANES spectra of O-Cu NW, FeN_4-O-Cu NW and reference samples (inset shows the enlarged Cu K-edge XANES spectra). b, Fourier transformed EXAFS spectra of Cu K-edge for O-Cu NW, FeN_4-O-Cu NW, and reference samples.

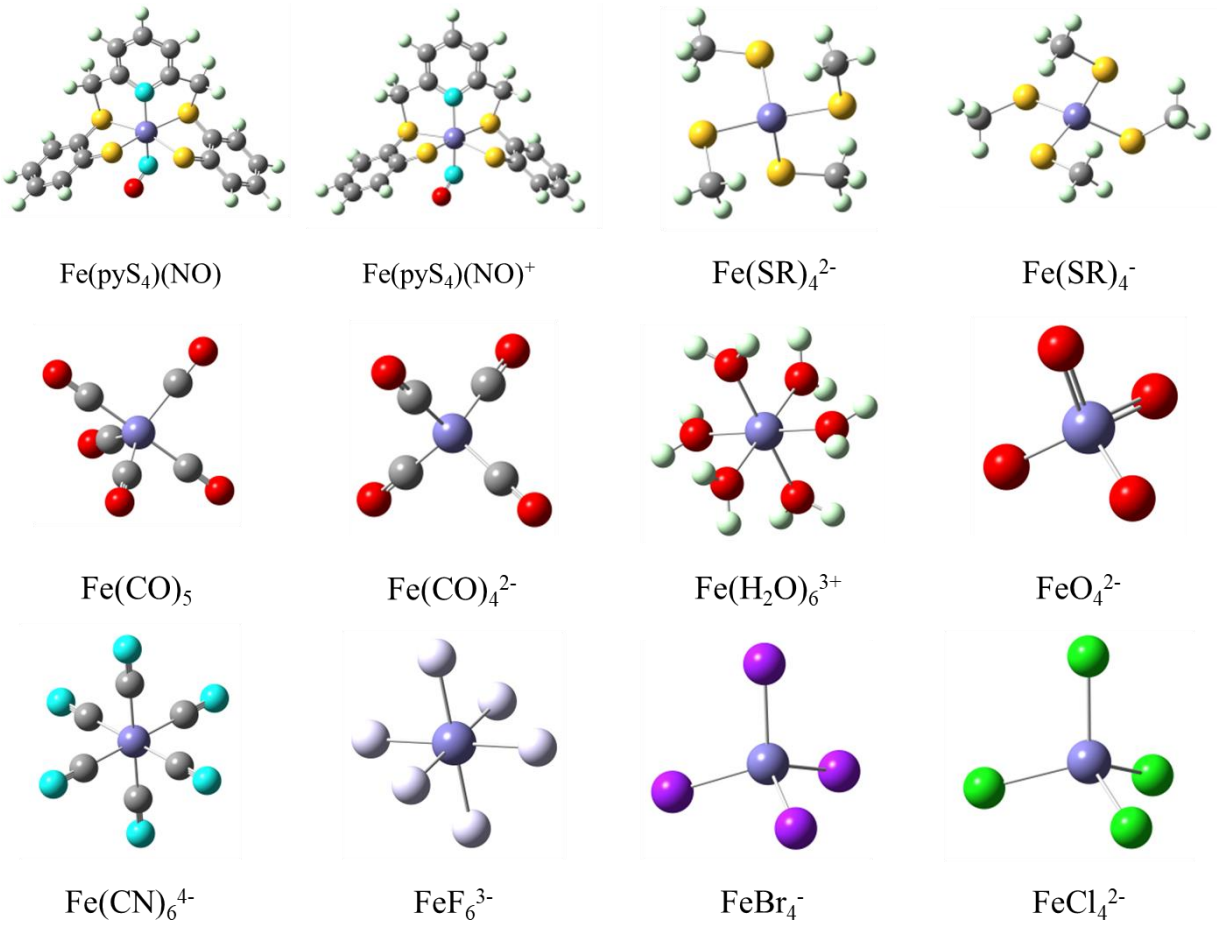

Supplementary Fig. 10 | The optimized Fe complexes for fitting the equation between electron density and IS, where the white, gray, blue, red, cyan, green, navy, dark red, and purple colors denote H, C, N, O, F, Cl, Fe, Br, and I atoms, respectively. The LS, MS, and HS represent low, medium, and high spin states of Fe atom, in which the corresponding labels are the most stable state compared to other spin states.

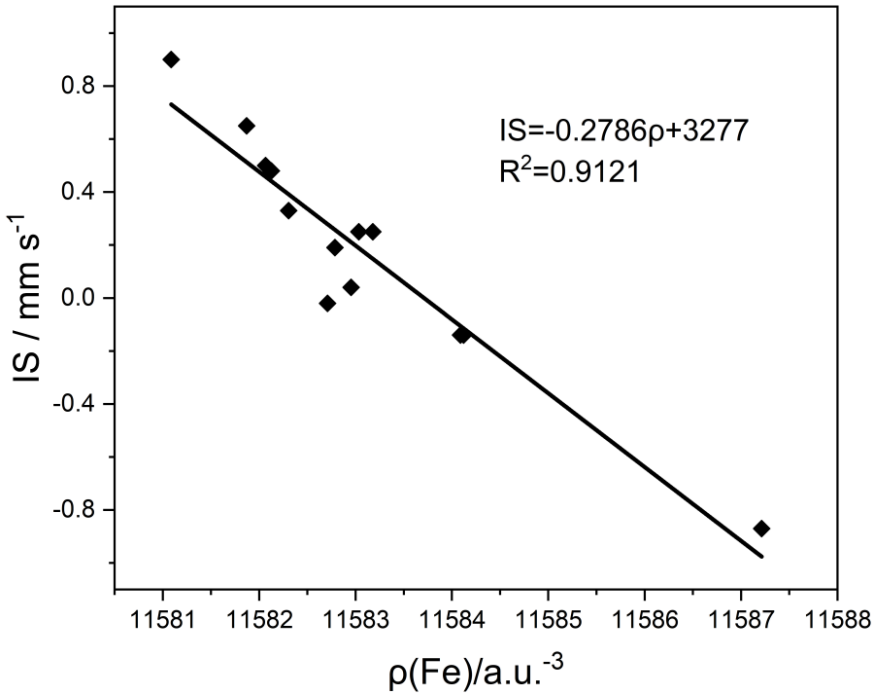

Supplementary Fig. 11 | The linear relationship between IS (mm s^{-1}) and electron density (ρ, a.u.^{3}) at the PBE0-D3(BJ)/def2-QZVP level of theory.

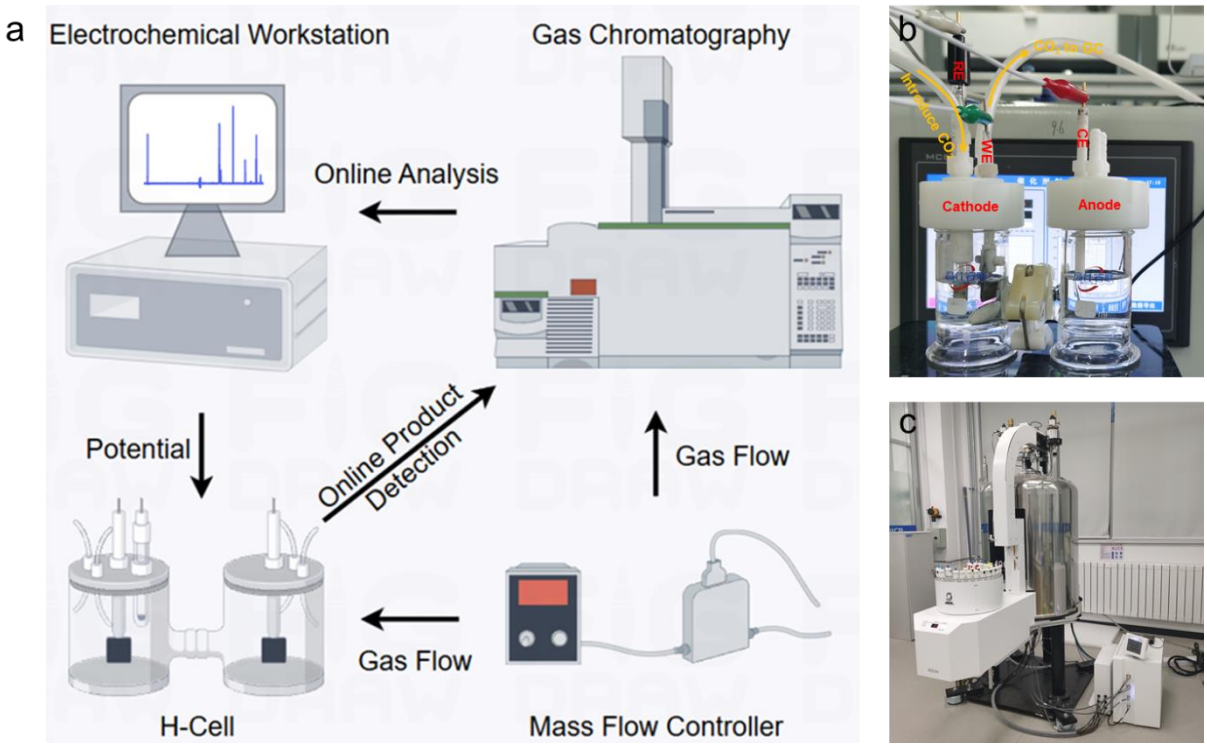

Supplementary Fig. 12 | a, Schematic diagram of online electrochemical CO_2 reduction technology route. b, An H-type electrochemical cell used for CO_2RR. WE: working electrode, CE: counter electrode, and RE: reference electrode. c, NMR used to quantify the liquid products.

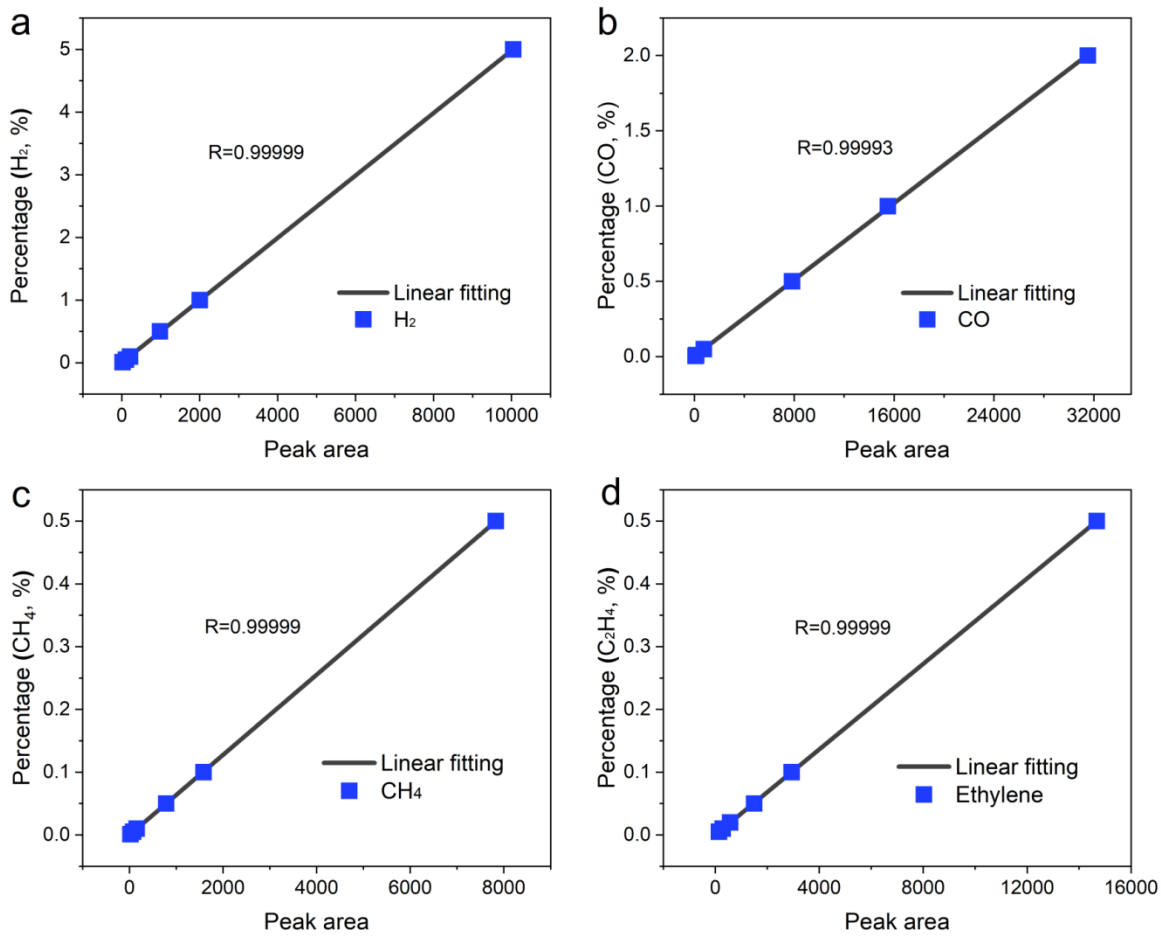

Supplementary Fig. 13 | Calibration curves based on the area of a, H_2, b, CO, c, CH_4, and d, C_2H_4 peak in the GC spectra.

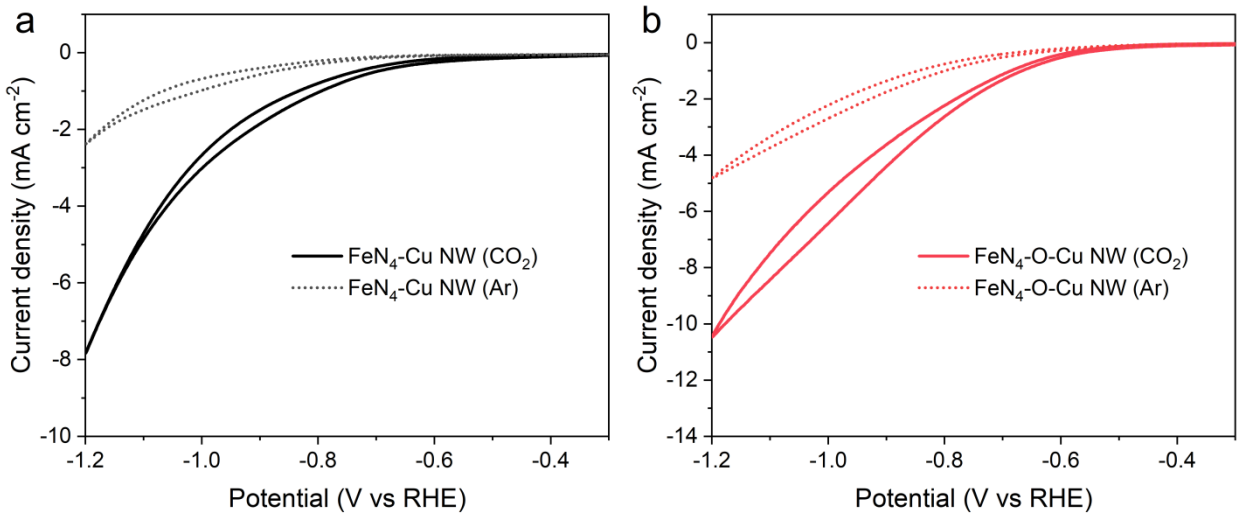

Supplementary Fig. 14 | a, b, CV curves of FeN_4-Cu NW, and FeN_4-O-Cu NW acquired in CO_2/Ar-saturated 0.5 M $KHCO_3$ solution on a rotating disc electrode at a rotation speed of 1600 rpm and a scan rate of 5 mV s^{-1}.

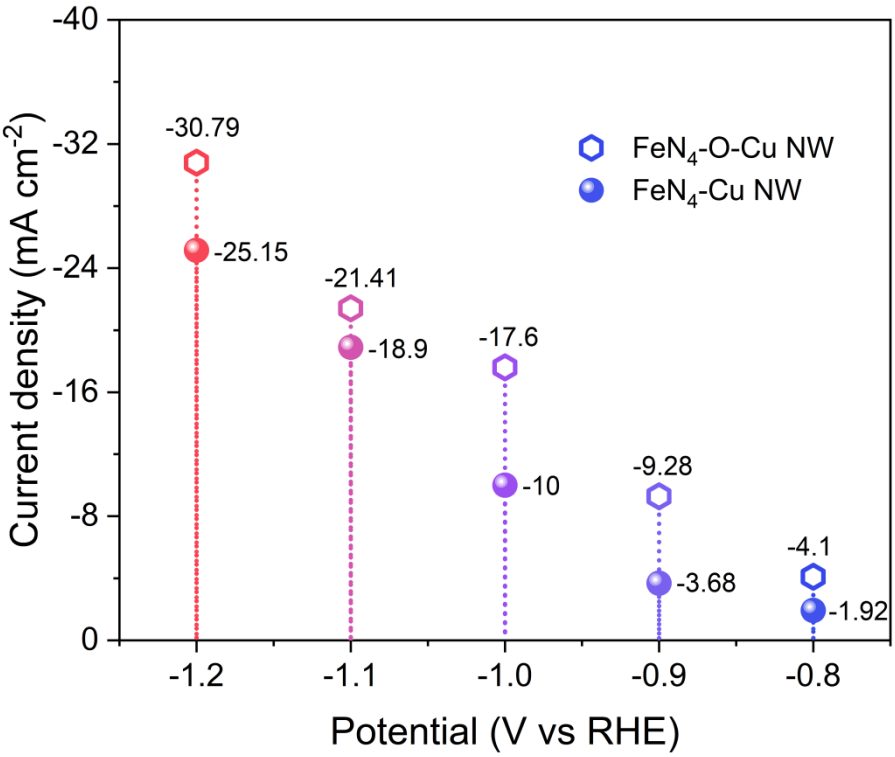

Supplementary Fig. 15 | Current density for FeN_4-Cu NW and FeN_4-O-Cu NW catalysts.

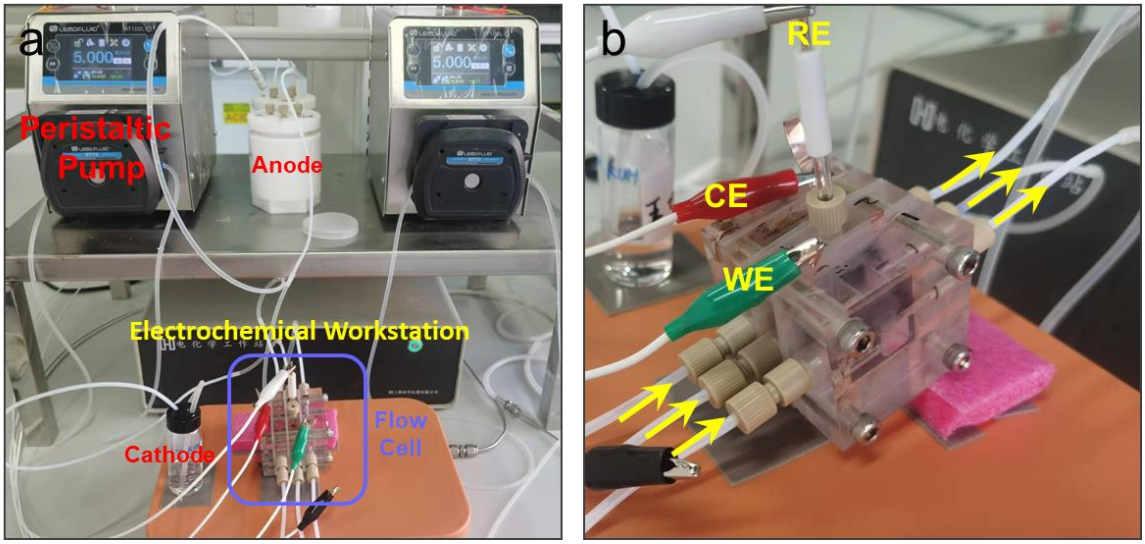

Supplementary Fig. 16 | a, Electrocatalytic CO_2 reduction Flow cell testing system. b, Flow-cell used for CO_2RR. WE: working electrode, CE: counter electrode, and RE: reference electrode.

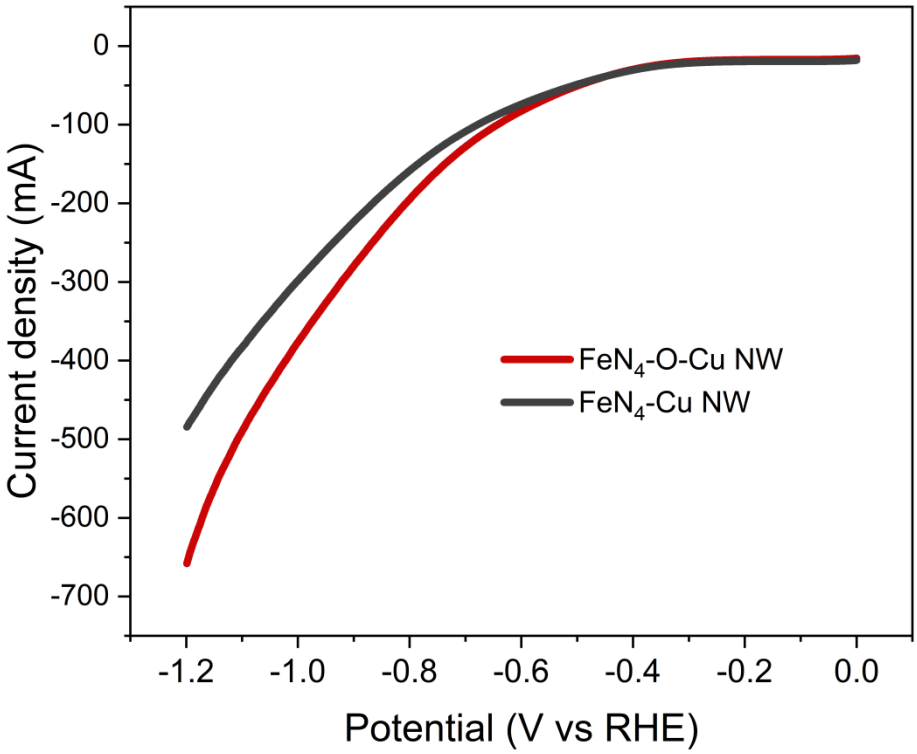

Supplementary Fig. 17 | LSV curves of FeN_4-Cu NW and FeN_4-O-Cu NW acquired in 1 M KOH on a GDE electrode at a scan rate of 5 mV s^{-1}.

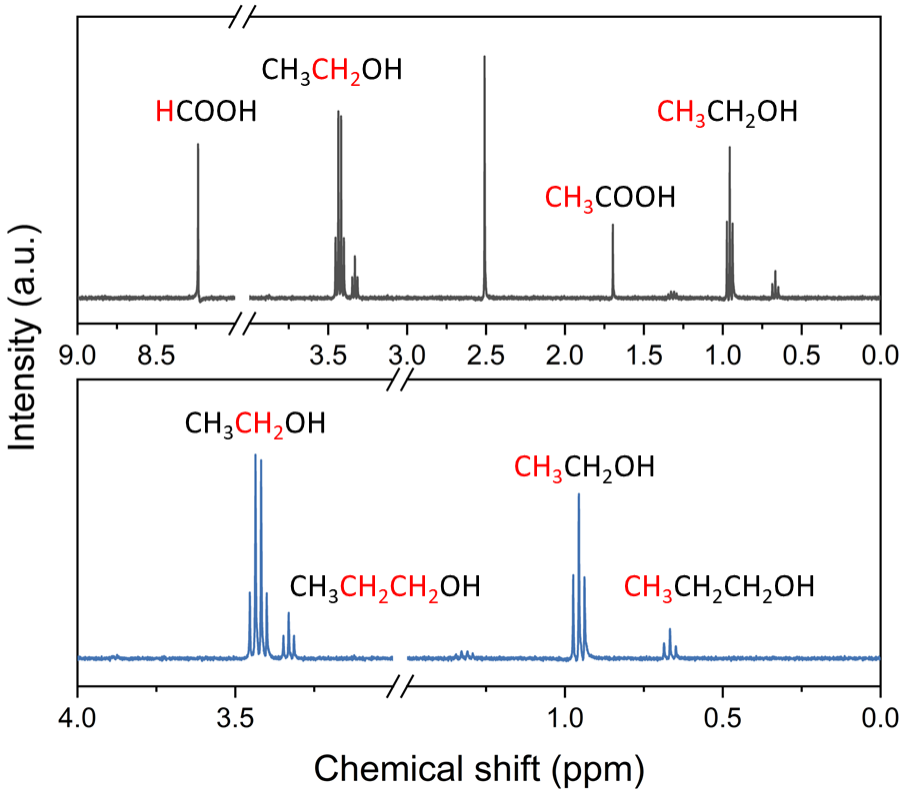

Supplementary Fig. 18 | ^{1}H NMR spectra to quantify liquid products for FeN_4-O-Cu NW at -1.0 V *vs.* RHE.

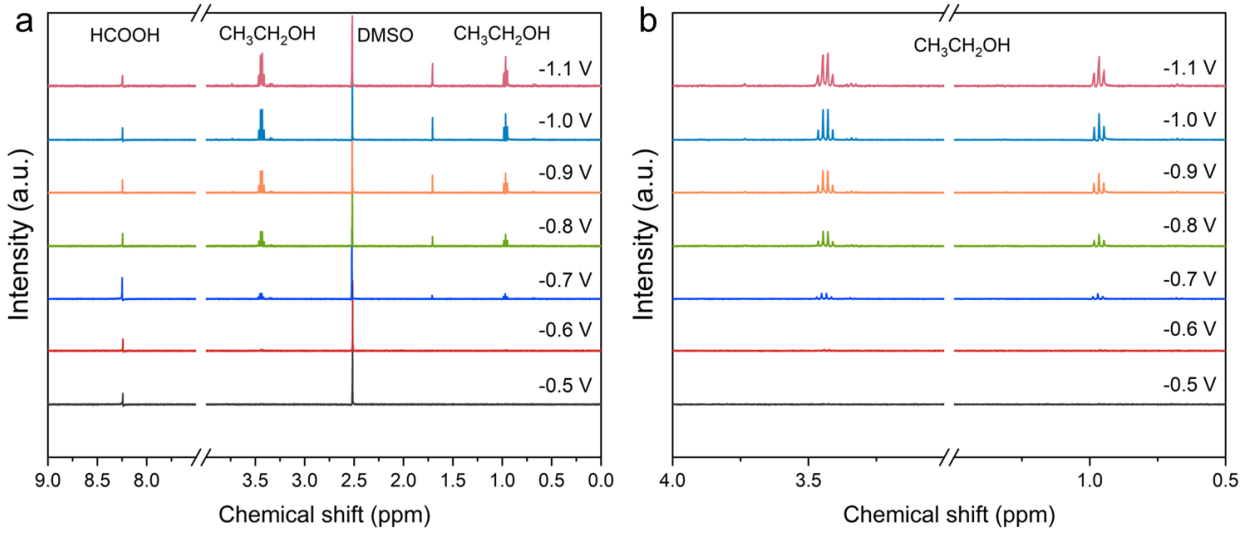

Supplementary Fig. 19 | ^{1}H NMR spectra of FeN_4-O-Cu NW in the potential range of -0.5 to -1.1 V *vs.* RHE.

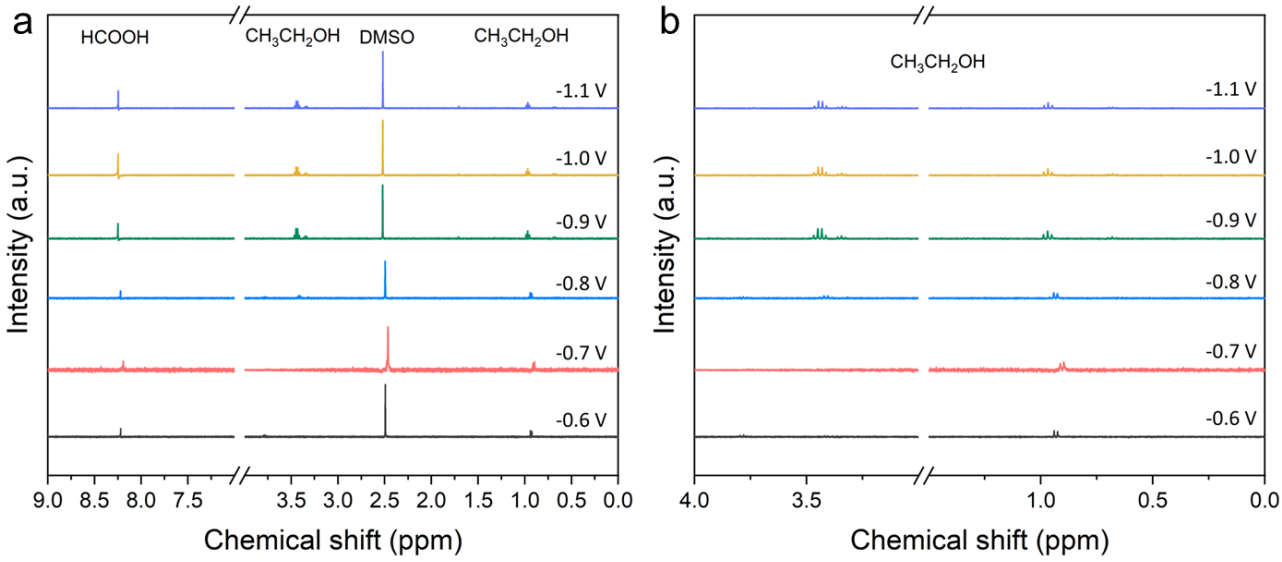

Supplementary Fig. 20 | ^{1}H NMR spectra of FeN_4-Cu NW in the potential range of -0.6 to -1.1 V *vs.* RHE.

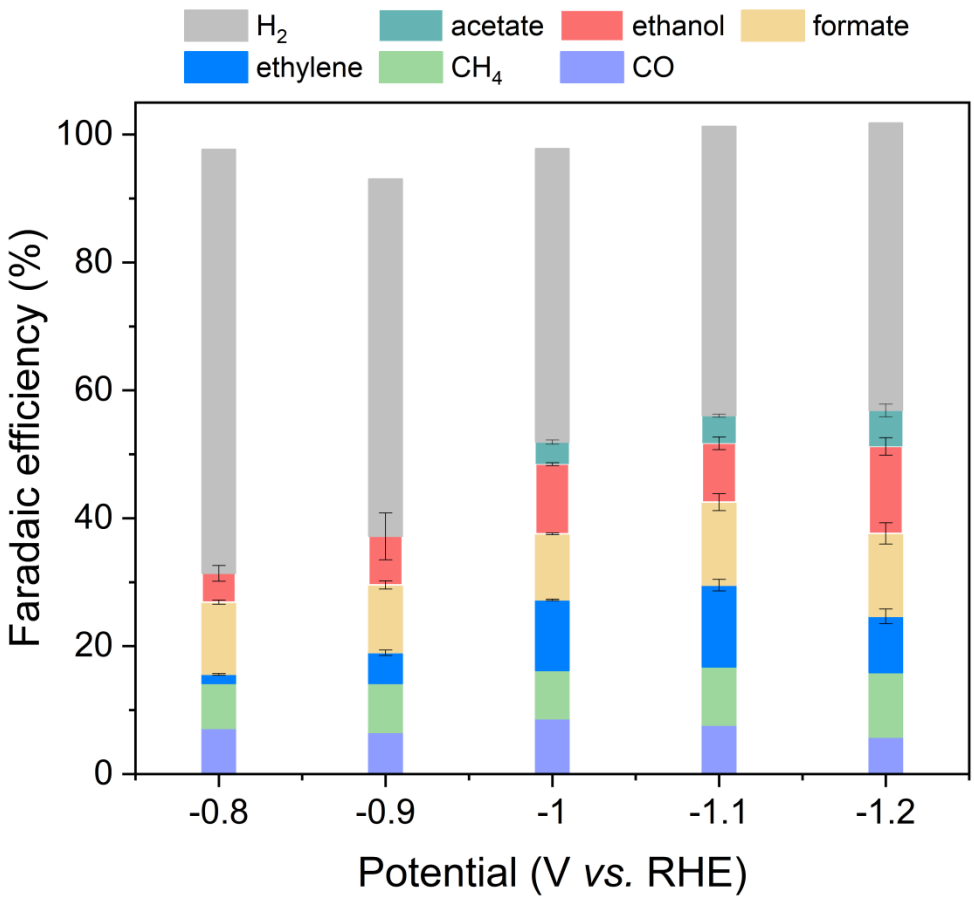

Supplementary Fig. 21 | Potential dependent Faradaic efficiencies for CO_2RR on O-Cu NW in an H-type cell.

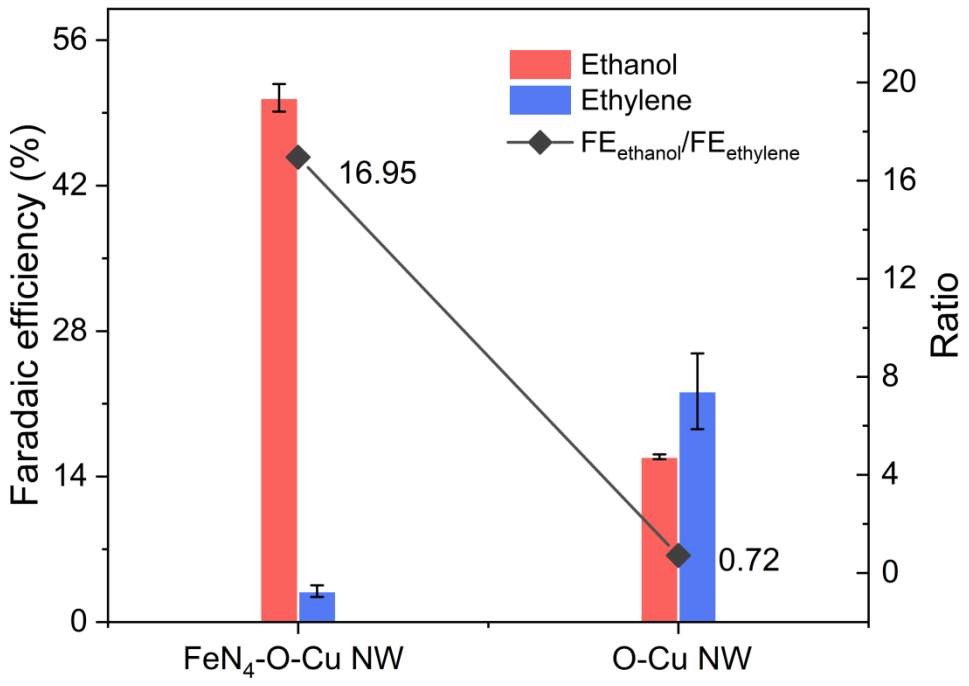

Supplementary Fig. 22 | The ethanol-to-ethylene Faradaic efficiency ratio ($FE_{ethanol}/FE_{ethylene}$) for FeN_4-O-Cu NW and O-Cu NW at -1.0 V *vs.* RHE.

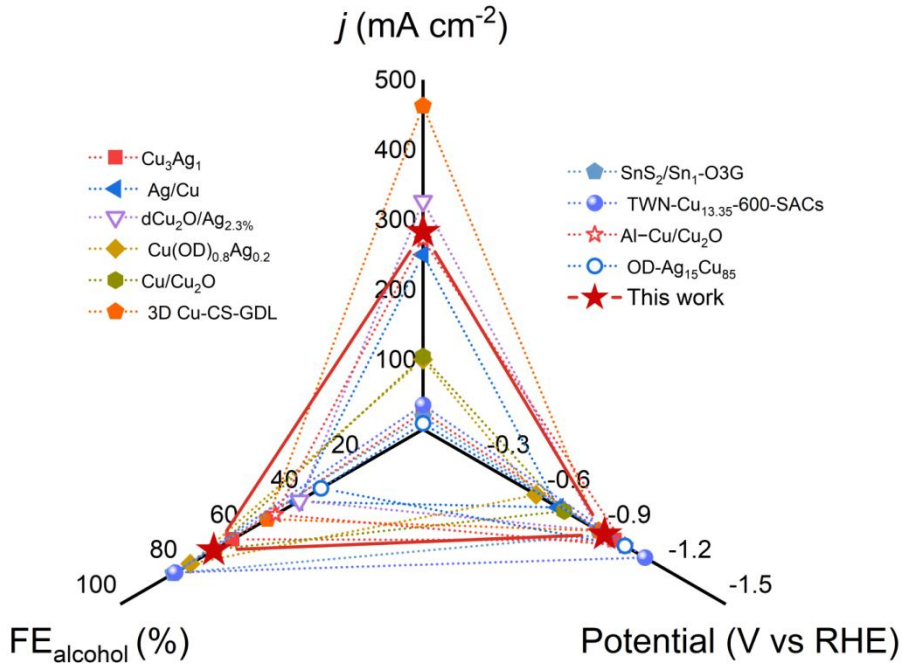

Supplementary Fig. 23 | Comparison of Faradaic efficiency and current density for CO_2RR to ethanol.

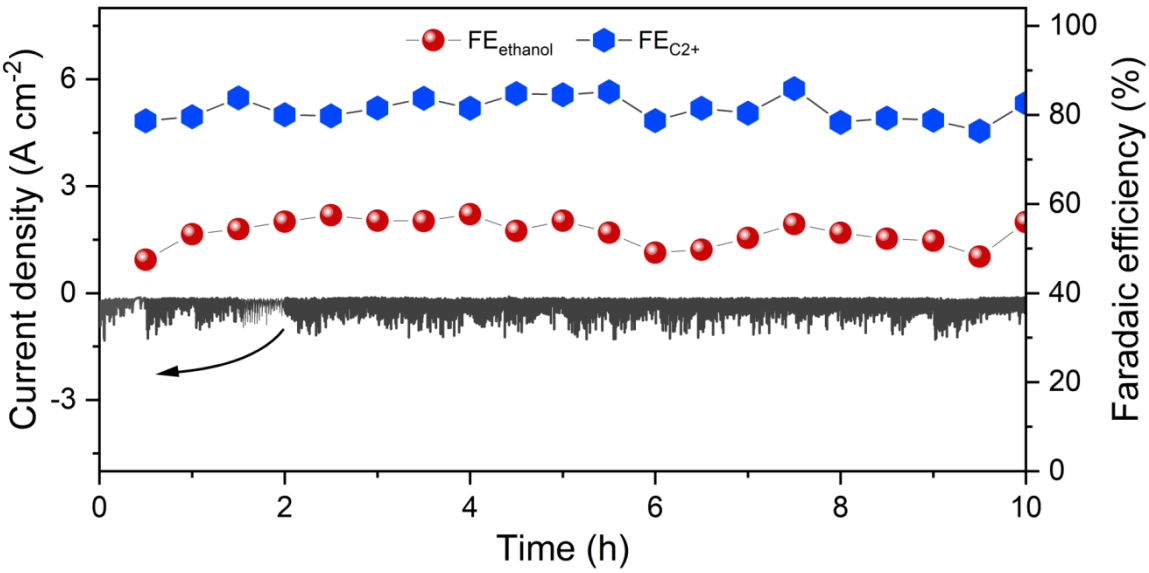

Supplementary Fig. 24 | The stability test of FeN_4-O-Cu NW acquired in a flow cell using 1 M KOH as the electrolyte at -0.9 V *vs.* RHE.

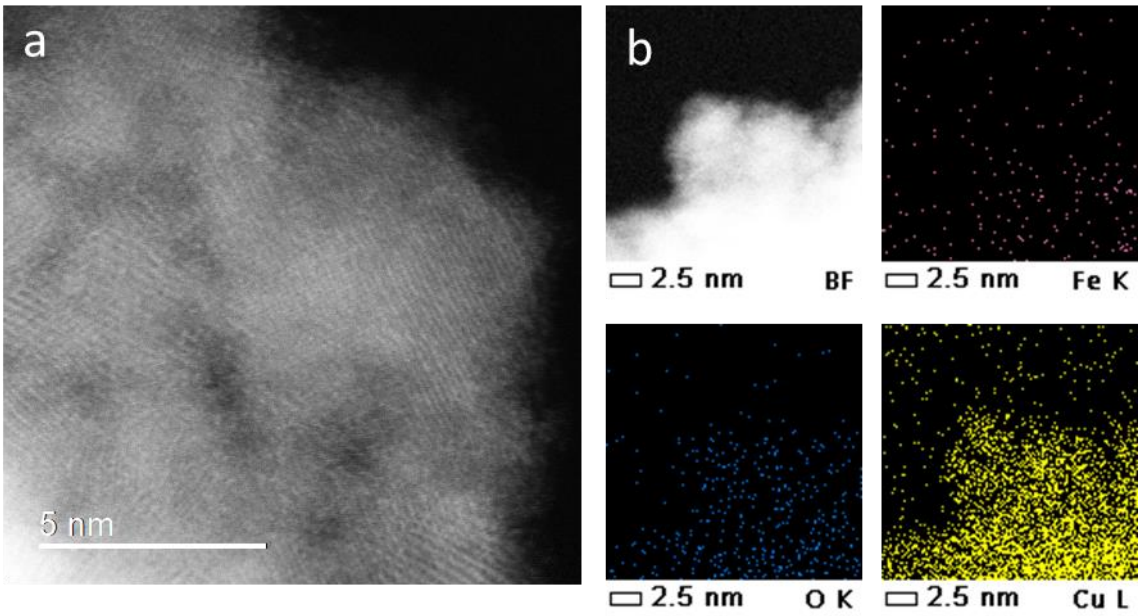

Supplementary Fig. 25 | a, HAADF-STEM images of FeN_4-O-Cu NW after CO_2RR. b, The EDX elemental mapping images of FeN_4-O-Cu NW after CO_2RR at high magnifications (2.5 nm).

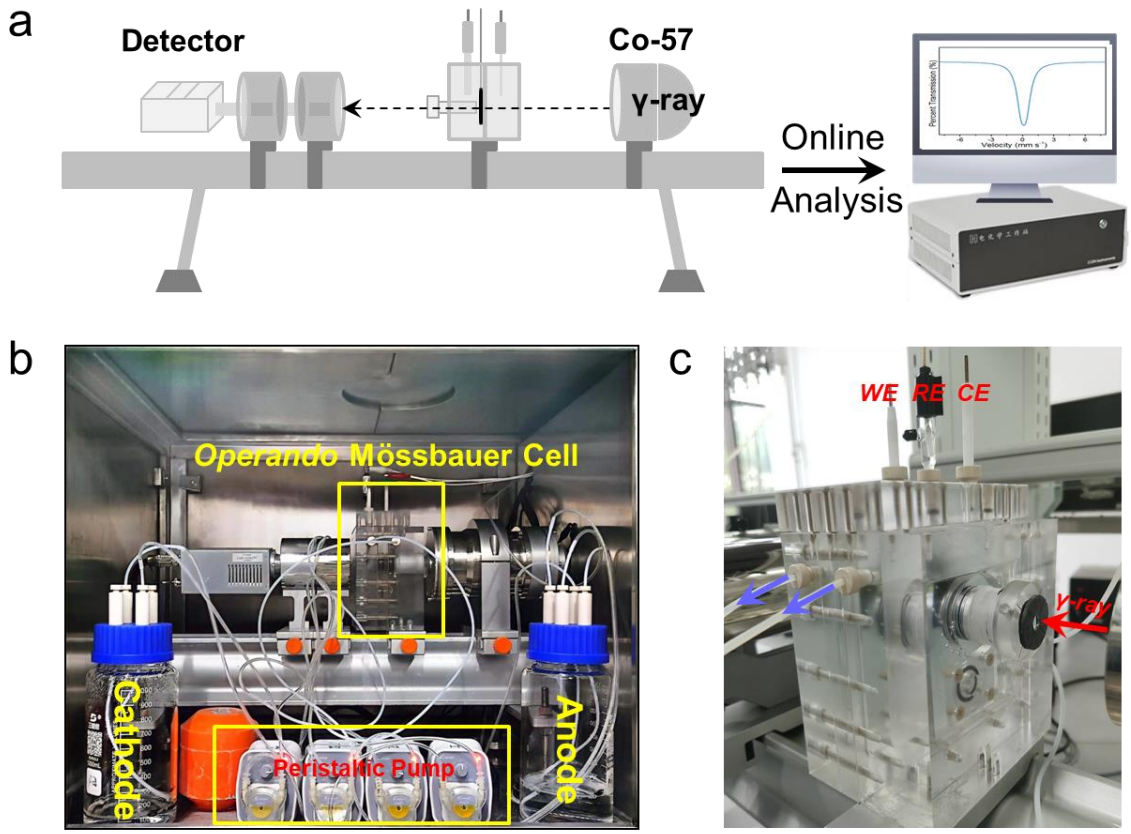

Supplementary Fig. 26 | a, Schematic diagram of electrochemical *operando* Mössbauer spectroscopy testing. b, Photograph of electrochemical *operando* Mössbauer spectroscopy. c, The detail of home-built *operando* Mössbauer cell. WE: working electrode, CE: counter electrode, and RE: reference electrode. To ensure a sufficient test duration, two large blue-mouthed bottles were utilized to hold over 500 mL of electrolyte solution. The anode and cathode electrolyte solutions were both 0.5 M $KHCO_3$, and the cathode electrolyte was saturated with CO_2 for 30 minutes before the measurement.

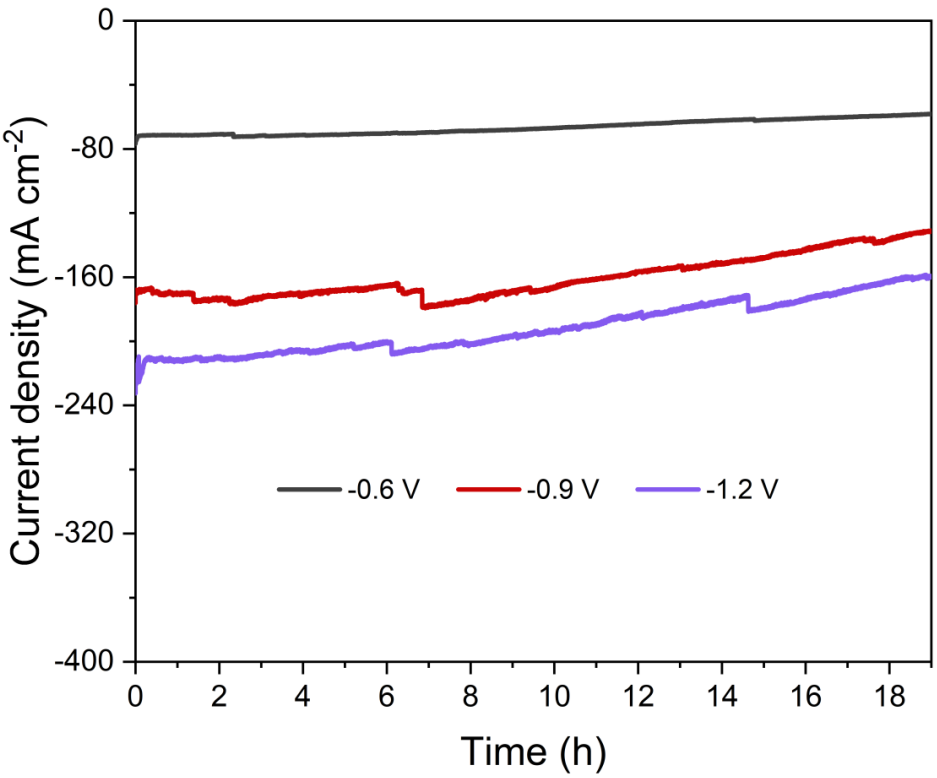

Supplementary Fig. 27 | Current-time response of FeN_4-O-Cu NW in *operando* ^{57}Fe Mössbauer measurements.

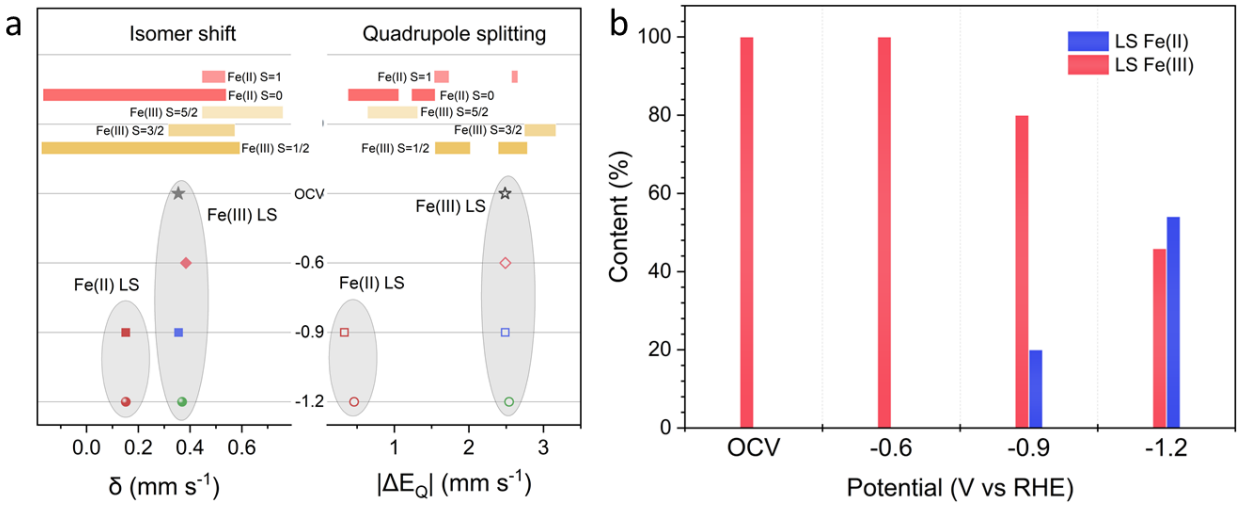

Supplementary Fig. 28 | a, The fitted parameters of operando ^{57}Fe Mössbauer spectra over FeN_4-O-Cu NW recorded at various applied cathodic potentials. **c**, The content of different Fe species under various potentials.

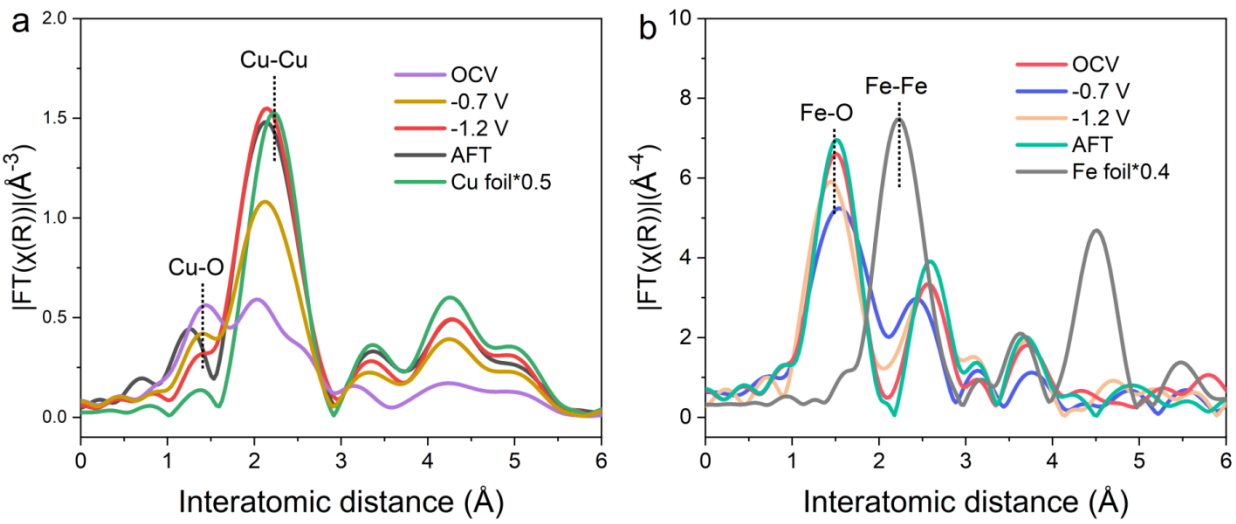

Supplementary Fig. 29 | a, b, *Operando* Cu K-edge and Fe K-edge EXAFS spectra during CO_2RR recorded in CO_2-saturated 0.5 M $KHCO_3$ solution.

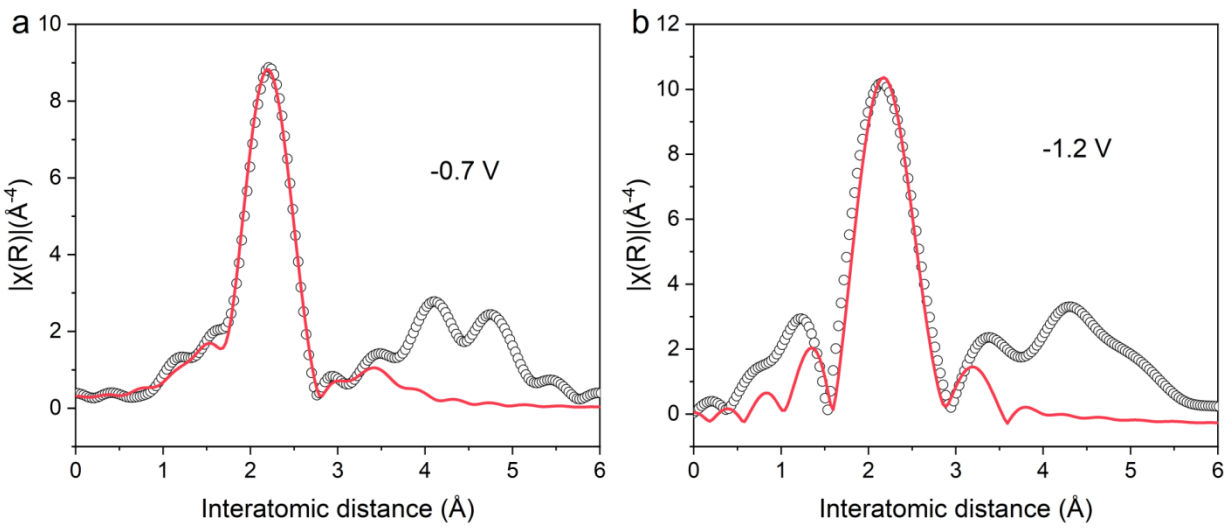

Supplementary Fig. 30 | EXAFS fitting curves in R space for FeN_4-O-Cu NW at -0.7 V and -1.2 V *vs.* RHE.

Further insights into the dynamic evolution of the catalyst under reaction conditions were obtained from EXAFS fitting (Supplementary Fig. 30). Additional fitting information can be found in Supplementary Table 8. To extract the detailed structural information from EXAFS, we analyzed the Cu–Cu and Cu-O path at -0.7 and -1.2 V *vs.* RHE. The Cu-Cu coordination number (CN) of FeN_4-O-Cu NW during the CO_2RR was quantified using the ARTEMIS program of IFEFFIT.

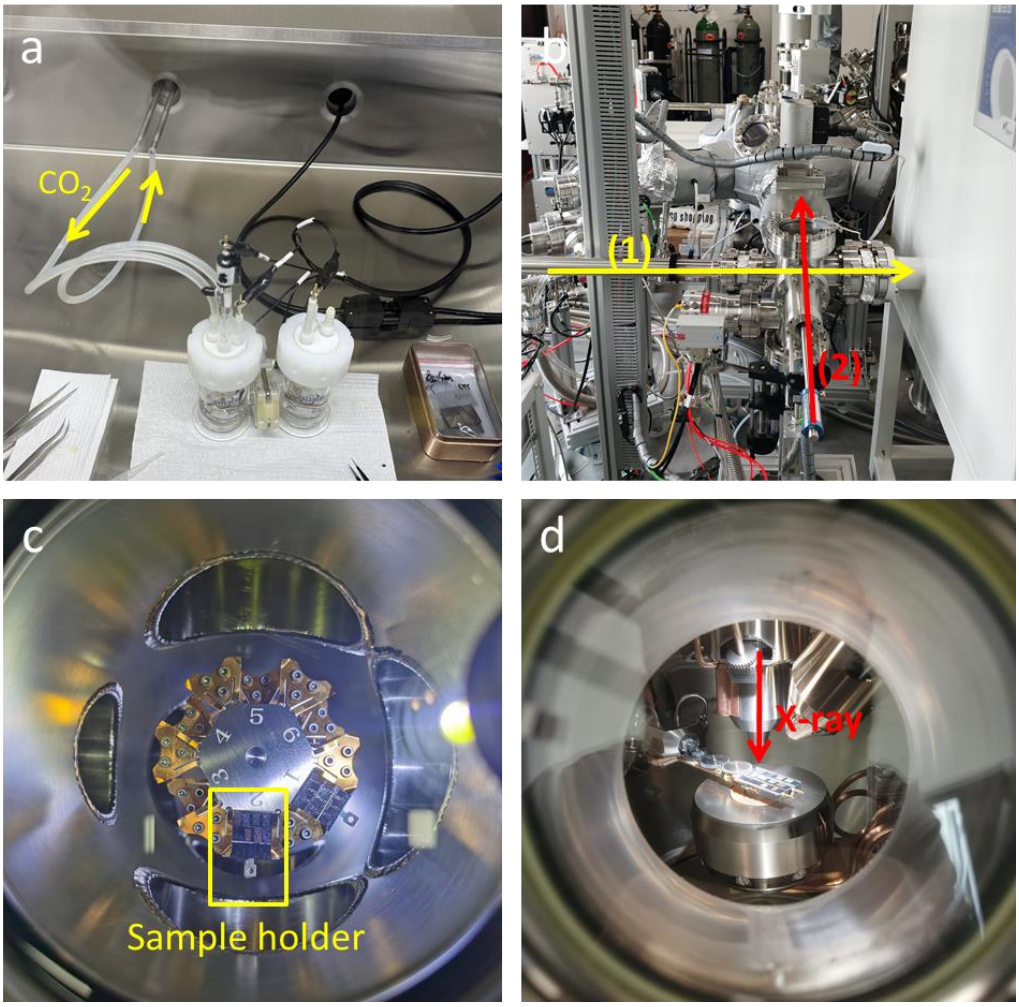

Supplementary Fig. 31 | a, Glovebox/XPS interconnected test system and H-type cell in glovebox used for CO_2RR. b, Vacuum-compatible sample transfer rod for transferring specimens from the glove box to the XPS analysis chamber. c, Sample transfer stage for vacuum XPS system. d, *Quasi in-situ* XPS sample under testing.

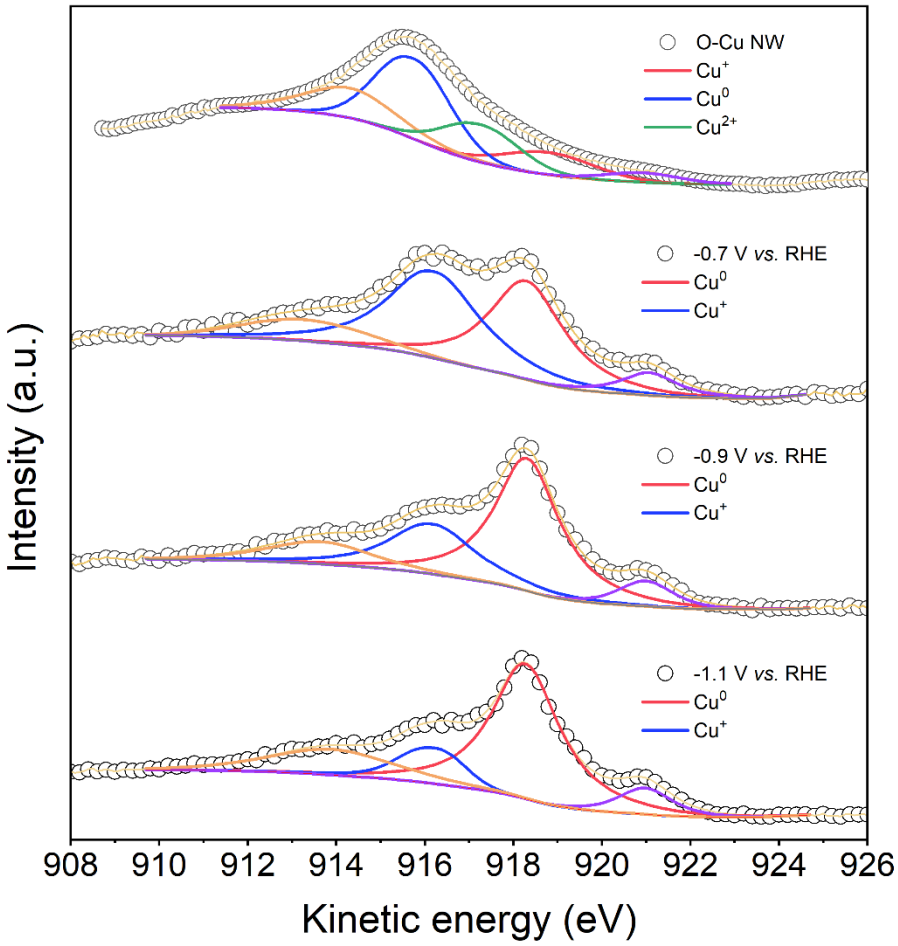

Supplementary Fig. 32 | Cu Auger spectra of O-Cu NW collected at the OCV, -0.7 to -1.1 V *vs.* RHE (ΔE = 0.2 V) in CO_2-saturated 0.5 M $KHCO_3$ electrolyte.

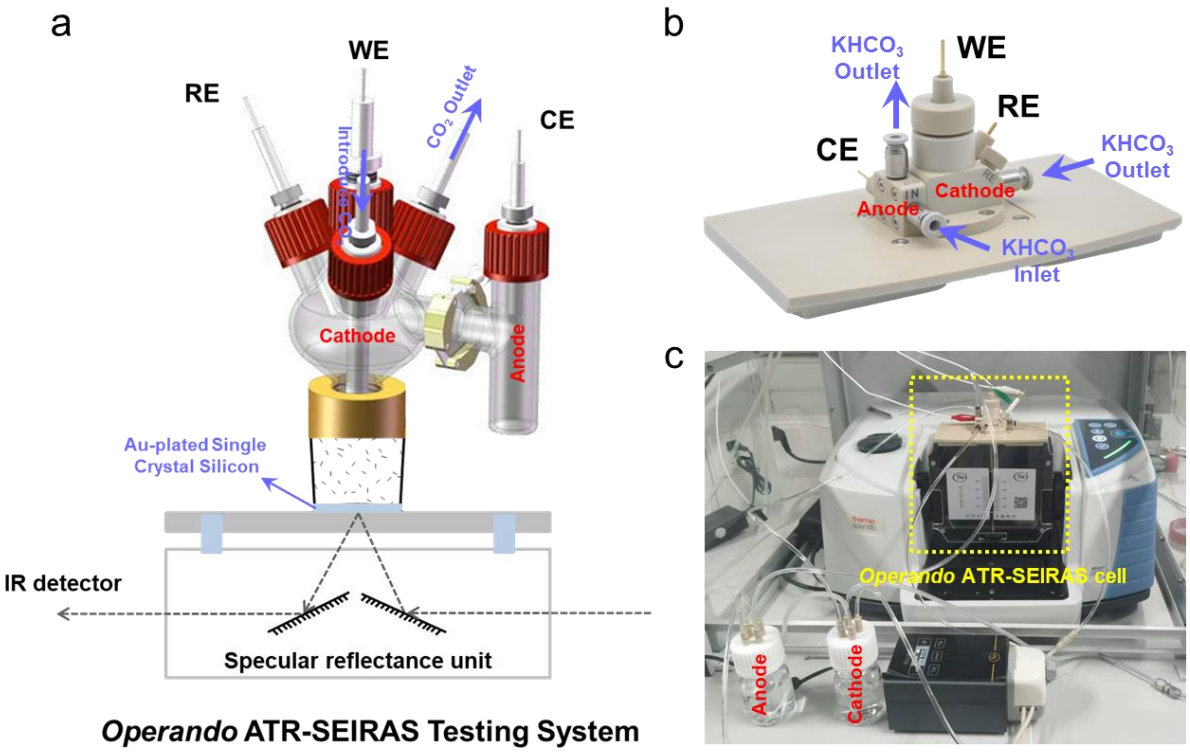

Supplementary Fig. 33 | a, Schematic diagram of the principle of *operando* electrochemical ATR-SEIRAS. b, c, *Operando* electrochemical ATR-SEIRAS spectroscopy reaction devices.

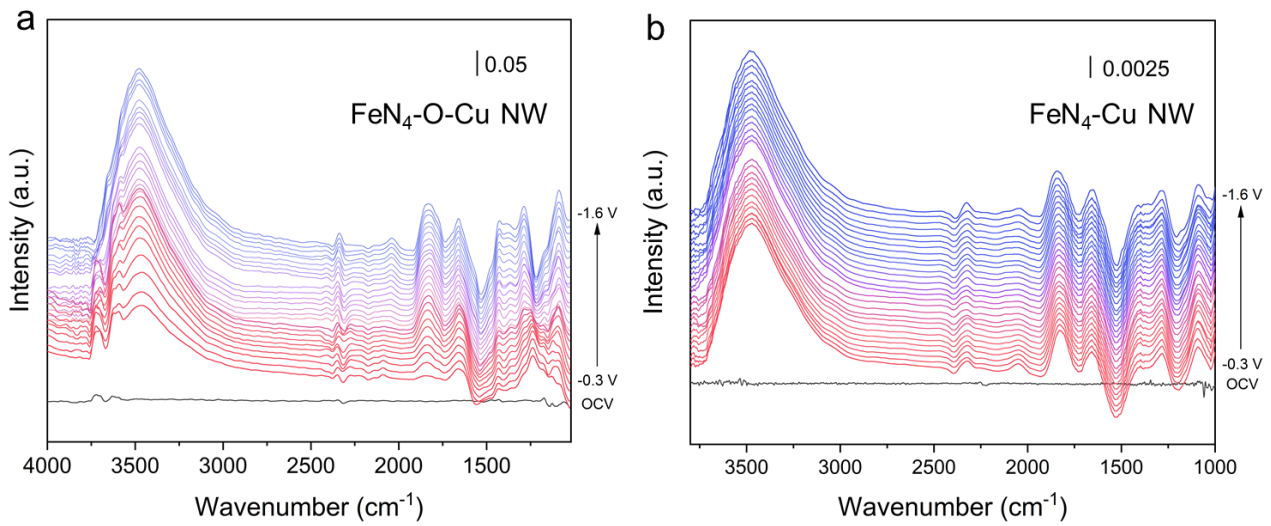

Supplementary Figs. 34 | a, b, *Operando* ATR-SEIRAS spectra collected in CO_2-saturated 0.1 M $KHCO_3$ solution at various potentials (V *vs.* RHE) over FeN_4-O-Cu NW and FeN_4-Cu NW, respectively.

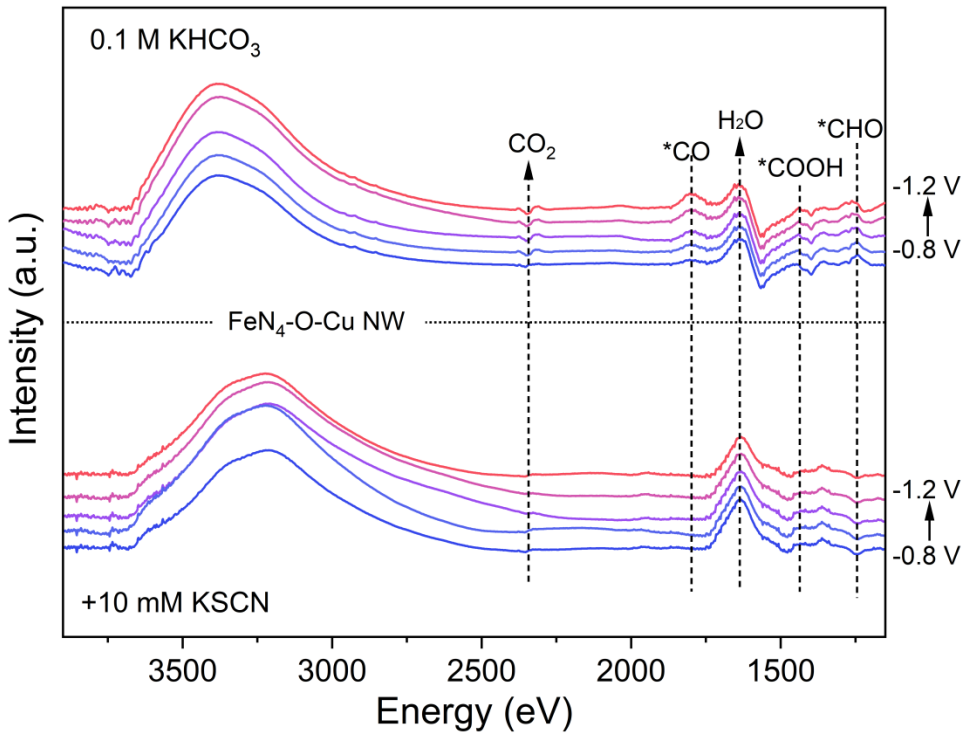

Supplementary Figs. 35 | *Operando* ATR-SEIRAS spectra collected in CO_2-saturated 0.1 M $KHCO_3$ solution with or without KSCN at various potentials (V *vs.* RHE) over FeN_4-O-Cu NW.

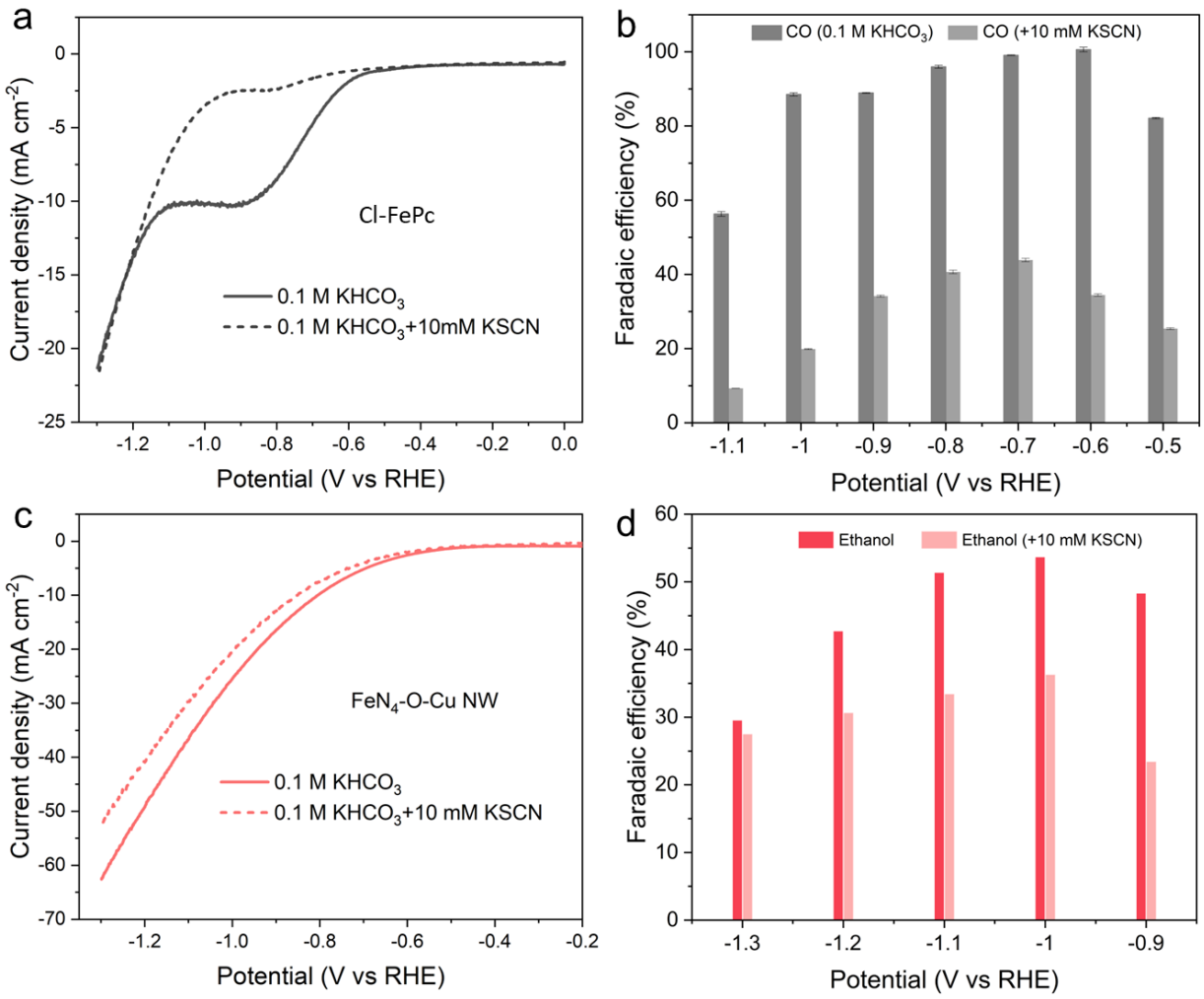

Supplementary Figs. 36 | a, c, LSV curves acquired in CO_2-saturated 0.1 M $KHCO_3$ solution with or without KSCN over Cl-FePc and FeN_4-O-Cu NW. **b**, **d**, Potential dependent Faradaic efficiencies for CO_2RR on Cl-FePc and FeN_4-O-Cu NW.

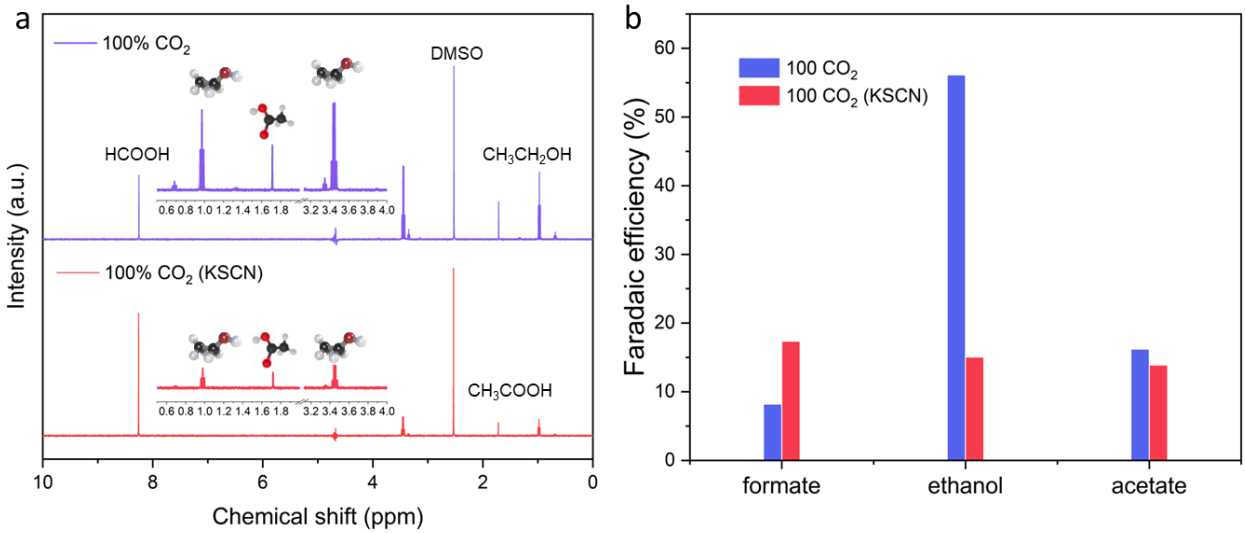

Supplementary Figs. 37 | a, ^{1}H NMR spectra of the electrolyte after electrolysis (E = -1.0 V *vs.* RHE, t = 1 h) in 100%CO_2 and 100%CO_2+KSCN-saturated electrolyte. **b**, Potential dependent C_2 Faradaic efficiencies for CO_2RR on FeN_4-O-Cu NW.

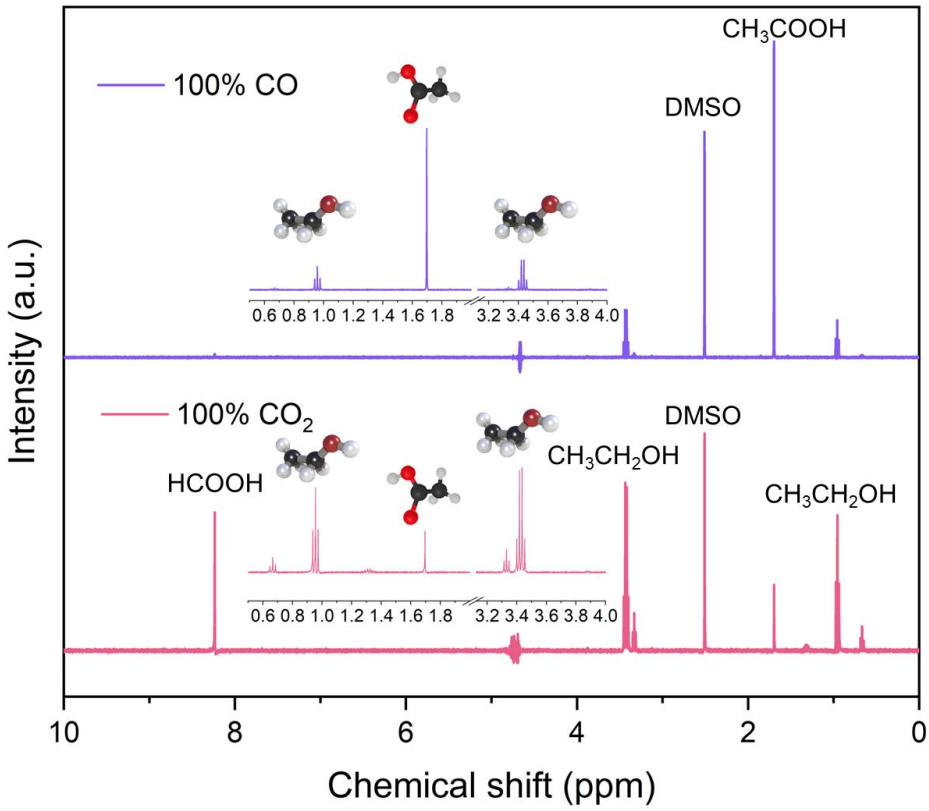

Supplementary Figs. 38 | ^{1}H NMR spectra of the electrolyte after electrolysis (E = -1.0 V *vs.* RHE, t = 1 h) in 100%CO_2 and 100%CO-saturated solutions.

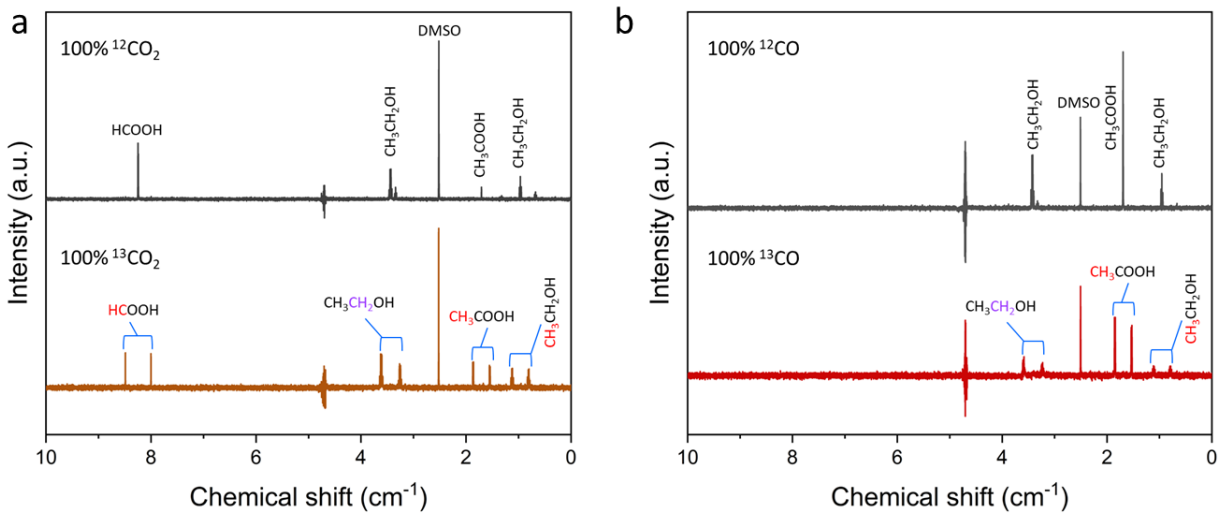

Supplementary Figs. 39 | The ^{1}H NMR patterns of ethanol produced from pure $^{13}CO_2/^{12}CO_2$ feeds and pure $^{13}CO/^{12}CO$ feeds.

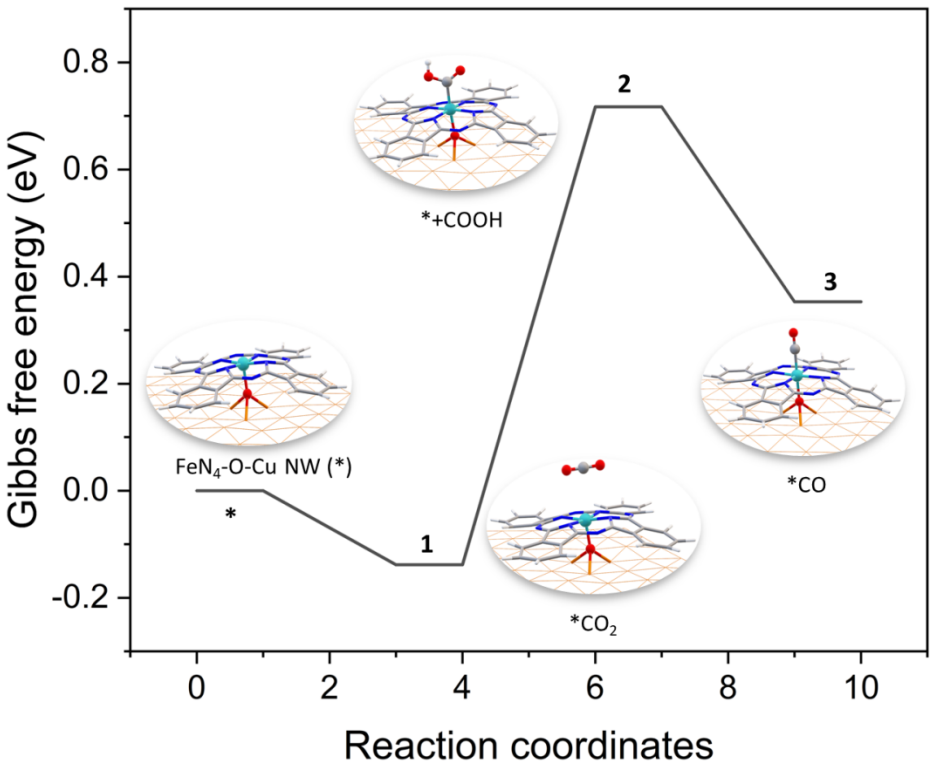

Supplementary Fig. 40 | Calculated Gibbs free energy profiles and optimized intermediate structures illustrating the CO_2RR pathway to CO at Fe sites over FeN_4-O-Cu NW catalysts.

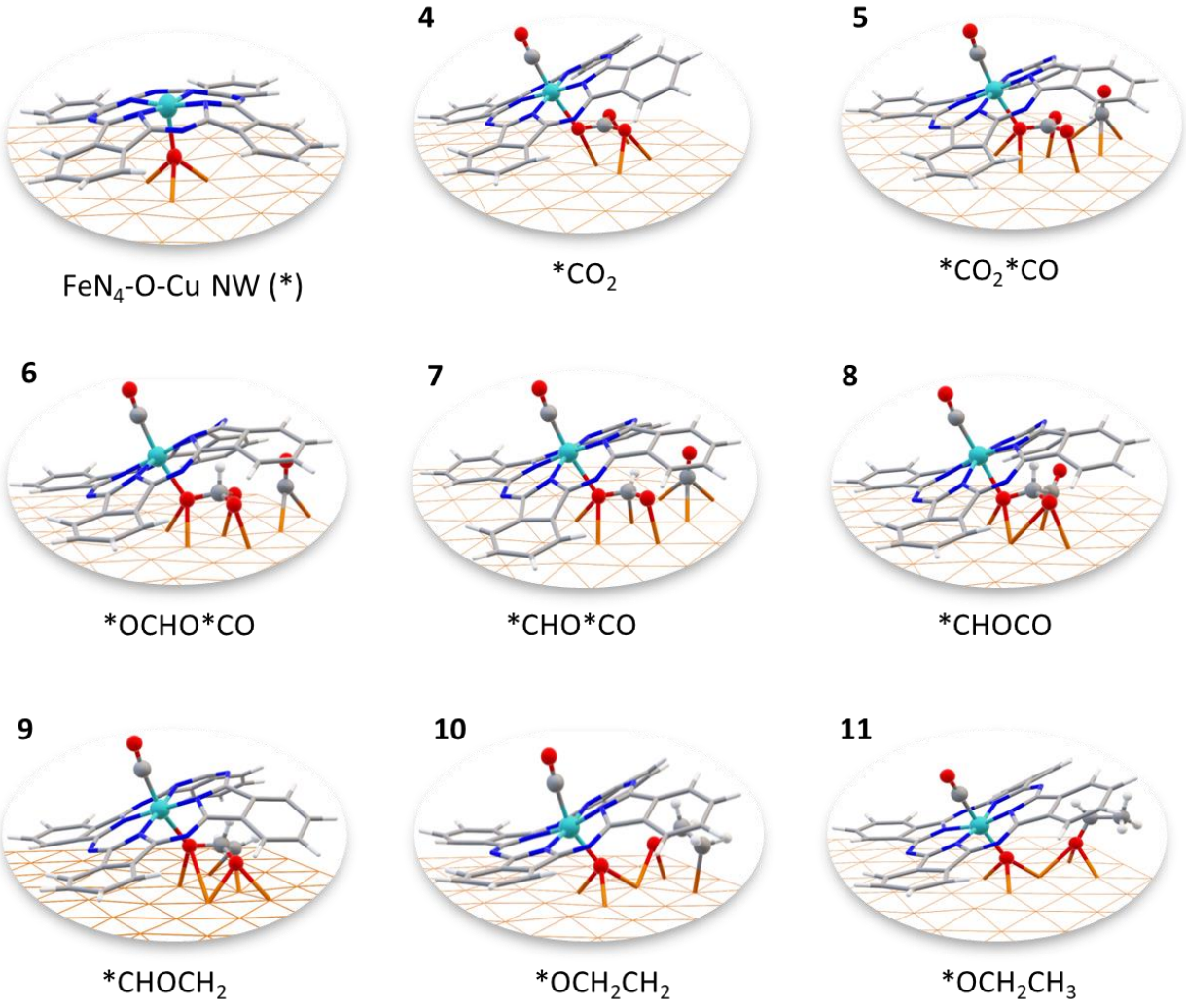

Supplementary Fig. 41 | Optimized intermediate structures illustrating the CO_2RR pathway to ethanol at O-bridged Fe-O-Cu sites over FeN_4-O-Cu NW catalysts.

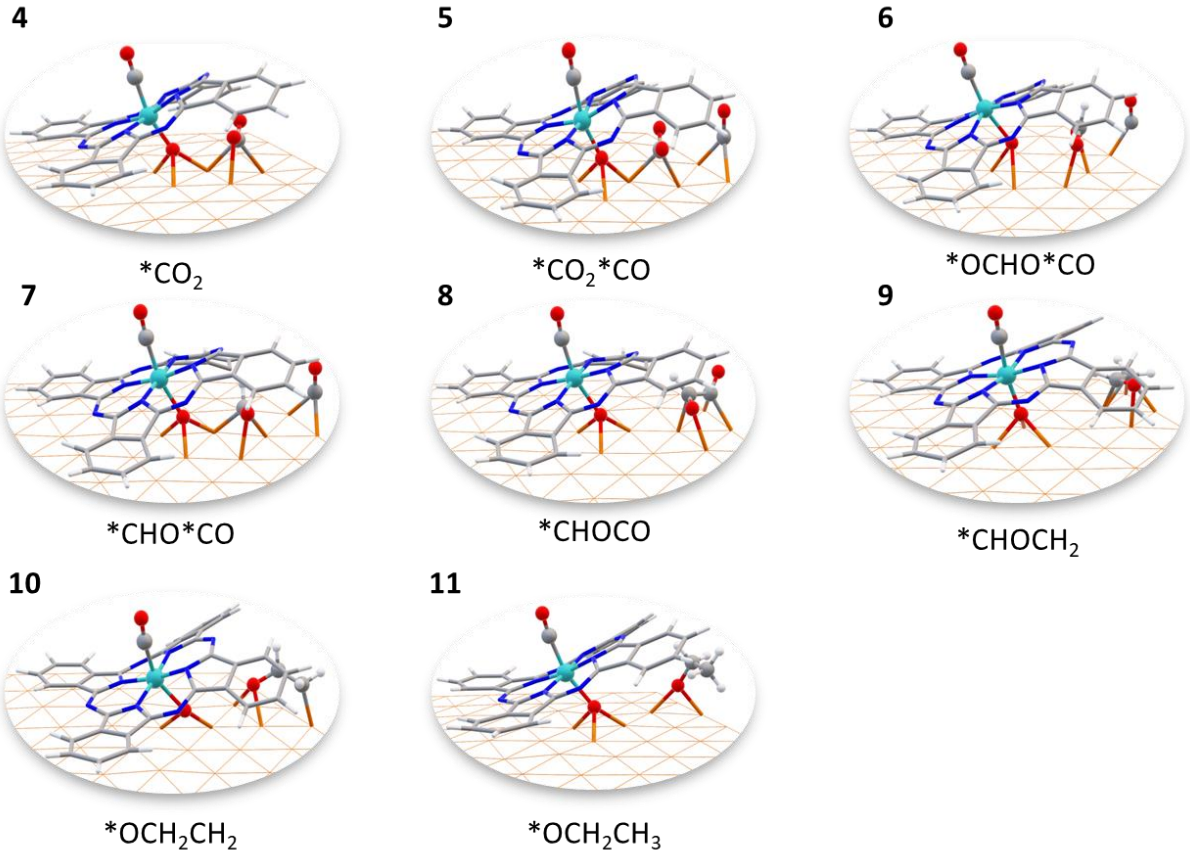

Supplementary Fig. 42 | Optimized intermediate structures illustrating the CO_2RR pathway to ethanol at Cu sites over FeN_4-O-Cu NW catalysts.

Supplementary Table 1 | Peak assignment for the IR for Cl-FePc[16,17].

Wavenumber (cm^{-1})	Assignment
730	Out-of-plane and in-plane C-H bond vibrations from the Pc ring
1076	
901	FeCl(Pc) reflects the metal-ligand vibrations
1116	Vibrations of C-H bend and benzene stretch and pyrole stretch, aza stretch
1162	and metal-N stretch
1132	C-C stretching vibrations from the isoindole structure
1714-1724	Stretching vibrations of C-C benzene and C-C pyrrole
809-813	C-H bending vibrations

Supplementary Table 2 | Peak assignment for the Raman spectrum for Cl-FePc[18-20].

Wavenumber (cm^{-1})	Assignment
483	Isoindole deformation
588	Benzene ring deformation
682	Macrocycle vibration, pyrrole expanding, benzene deformation
750	C-N-C, N-Fe stretching
777	Isoindole N-Fe stretching
825	Pyrrole N-Fe stretching, benzene expanding, C−N−C in-plane bending
946	N-Fe, C-N-C in-plane bending, isoindole deformation
1107	C-H in-plane bending, isoindole N−Fe stretching
1143	Pyrrole breathing
1398	Ring breathing caused by O_2 adsorption
1451	Isoindole stretching, ring stretching, pyrrole N-Fe, C-H in-plane bending

Supplementary Table 3 | ICP results of O-Cu NW, FeN_4-Cu NW and FeN_4-O-Cu NW.

Samples	O-Cu NW	FeN_4-O-Cu NW	FeN_4-Cu NW
Fe wt.%	0	0.65	0.73

Supplementary Table 4 | The fitted parameters of *ex situ* ^{57}Fe Mössbauer spectra of as-synthesized ^{57}FePcCl, and $^{57}FeN_4$-O-Cu NW.

Sample	Component	IS (mm s^{-1})	QS (mm s^{-1})	Γ (mm s^{-1})	Area (%)
^{57}FePcCl	LS Fe(III)	0.19	2.71	0.56	100.0
$^{57}FeN_4$-O-Cu NW	LS Fe(III)	0.37	2.48	0.34	100.0

Experimental errors for isomer shift (IS), and quadrupole splitting (QS) are ± 0.003 mm s^{-1}, ± 0.007 mm s^{-1}, respectively. The IS is given relative to α-iron foil.

Supplementary Table 5 | The electron density (a.u.^{3}) of Fe atom at PBE0 functional and def2-QZVP basis set, and their experimental IS (mm s^{-1}) values[21].

Molecules	Spin	ρ(Fe)/a.u.$^{-3}$	QS	IS/mm s^{-1}
$Fe(SR)_4^{2-}$	M	11581.87032	0.032455	0.65
$Fe(pyS_4)(NO)$	L	11582.30694	0.53253	0.33
$Fe(SR)_4^{-}$	M	11583.1786	3.262197	0.25
$Fe(pyS_4)(NO)^{+}$	L	11582.95343	1.460799	0.04
FeO_4^{2-}	L	11587.21343	4.025094	-0.87
$Fe(H_2O)_6^{3+}$	H	11582.06749	-0.015431	0.5
$Fe(CN)_6^{4-}$	L	11582.70892	0.000053	-0.02
$Fe(CO)_4^{2-}$	M	11584.0896	1.216171	-0.14
$Fe(CO)_5$	L	11584.12267	2.180503	-0.14
$FeCl_4^{-}$	H	11582.78659	-1.734212	0.19
$FeCl_4^{2-}$	H	11581.08798	3.020257	0.9
$FeBr_4^{-}$	H	11583.03477	0.003399	0.25
FeF_6^{3-}	H	11582.12633	0.000007	0.48

Calculated electron density ρ(Fe) at the nucleus and the corresponding IS from experiments. The reference is α-Fe.

Supplementary Table 6 | Comparison of ethanol yield from CO_2RR on different electrocatalysts.

Samples	Current density ($mA\ cm^{-2}$)	Potential (V vs. RHE)	Electrolyte	Product	FE (%)	References
FeN_4-O-Cu NW	282.5	-0.9	1 M KOH	ethanol	57.3	This work
Cu=N catalyst	406	-0.82	1 M KOH	ethanol	45	J. Am. Chem. Soc. 2024, 146, 20, 14260-14266 (Ref [22])
Ag/Cu	250	-0.67	1 M KOH	ethanol	41.4	J. Am. Chem. Soc. 2019, 141, 8584 (Ref [23])
B-NiO	1.21	-0.6	1 M $KHCO_3$	ethanol	75.2	Adv. Mater. 2024, 36, 2410125 (Ref [24])
AgCu wire	300	-0.7	1 M KOH	ethanol	25	J. Am. Chem. Soc. 2018, 140, 5791 (Ref [25])
$dCu_2O/Ag_{2.3\%}$	326.4	-0.87	1 M KOH	ethanol	40.8	Nat. Commun. 2022, 13, 3754 (Ref [26])
SnS_2/Sn_1-O3G	17.8	-0.9	0.5 M $KHCO_3$	ethanol	82.5	Nat Energy 2023, 8, 1386-1394 (Ref [27])
Ag/Cu_2O	12.5	-1.0	0.1 M $KHCO_3$	alcohol	30	Angew. Chem. Int. Ed. 2021, 60, 7426 (Ref [28])
Cu/Cu_2O sheet	103.9	-0.7	2 M KOH	ethanol	68.8	Nat. Commun. 2023, 14, 501 (Ref [29])
TWN-$Cu_{13.35}$-600-SACs	35.6	-1.1	0.5 M $CsHCO_3$	ethanol	81.9	J. Am. Chem. Soc. 2023, 145, 31, 17253-17264 (Ref [30])
CuOCu-N_4	10.76	-0.3	1 M KOH	ethanol	56.3	J. Am. Chem. Soc. 2024, 146, 13, 9365-9374 (Ref

						[31])
$Cu(OD)_{0.8}Ag_{0.2}$	~100	-0.56	1 M KOH	ethanol	76.9	Nat. Commun. 2023, 14, 698 (Ref [32])
CeO_2/CuO	344	-1.5	0.5 mM H_2SO_4 and 3 M KCl	ethanol	48.5	Angew. Chem. Int. Ed. 2025, 64, e202424248 (Ref [33])
$Ce(OH)_x$/Cu/PTFE	128	-0.7	1 M KOH	ethanol	43	Nat Commun 2019, 10, 5814 (Ref [34])
OD-$Ag_{15}Cu_{85}$	8.67	-1.0	0.5 M $KHCO_3$	ethanol	33.7	Nano Energy 2020, 68, 104331 (Ref [35])

Supplementary Table 7 | The fitted parameters of *operando* ^{57}Fe Mössbauer spectra over $^{57}FeN_4$-O-Cu NW recorded at various applied cathodic potentials.

Potential	Assignment	IS (mm s^{-1})	QS (mm s^{-1})	Magnetic field (kOe)	Γ (mm s^{-1})	Area (%)
CO_2 (OCV)	LS Fe(III)	0.35	2.48	-	0.29	100.0%
CO_2 (-0.7 V)	LS Fe(III)	0.38	2.48	-	0.30	80.0%
	LS Fe(II)	0.15	0.33	-	0.58	20.0%
CO_2 (-1.2 V)	LS Fe(III)	0.36	2.54	-	0.29	45.9%
	LS Fe(II)	0.15	0.46	-	0.58	54.1%

Experimental errors for isomer shift (IS), quadrupole splitting (QS) and relative area are ± 0.02 mm s^{-1}, ± 0.08 mm s^{-1} and less than 3%, respectively. IS is given relative to α-iron foil.

Supplementary Table 8| Structural parameters of FeN_4-O-Cu NW extracted from the Cu K-edge EXAFS fitting.

Sample	Path	CN	R(Å)	ΔE(eV)	DW	R-factor
Cu foil	Cu-Cu	12	2.54	4.709	0.008	0.002
-0.7 V	Cu-Cu	6.59	2.53	1.95	0.012	0.006
	Cu-O	3.61	1.86	1.95	0.007	0.006
-1.2 V	Cu-Cu	5.58	2.53	0.44	0.008	0.009
	Cu-O	2.22	1.86	0.44	0.013	0.009

Supplementary Table 9 | Quantitative analysis of Cu speciation through corresponding Cu Auger spectra.

Catalysts	Potential (V vs. RHE)	Faradaic efficiency (ethanol, %)	Cu^0 (%)	Cu^+ (%)	Cu^{2+} (%)	Cu^+/Cu^0
FeN_4-O-Cu NW	OCV	/	29.6	44.8	25.6	/
	-0.7	26.3	81.3	23.6	0	0.29
	-0.9	57.3	70.9	29.1	0	0.41
	-1.1	48.3	73.6	26.5	0	0.36
O-Cu NW	OCV	/	18.8	55.2	26.0	/
	-0.7	4.5	48.2	51.8	0	1.08
	-0.9	7.6	62.1	37.9	0	0.61
	-1.1	9.2	82.0	18.0	0	0.22

Supplementary Table 10 | Summary of IR spectra (cm^{-1}) for various carbonate and intermediate species captured in CO_2RR.

This work	Wavenumber (cm^{-1})	Species	Reference
2345	~2330-2350	CO_2	*Nat. Commun.* 2022, 13, 6082 (Ref [38])
1620	~1630-1660	H_2O/O-H	*Angew. Chem. Int. Ed.* 2022, 61, e202209268 (Ref [39])
1462-1541	~1458-1535	CO_3^{2-}	*ACS Energy Lett.* 2019, 4, 682−689 (Ref [40]) *Nat. Commun.* 2022, 13, 6082 (Ref [38])
~2050	~1950-2100	*CO atop	*Energy Environ. Sci.* 2022, 15, 2397-2409 (Ref [41])
~1865	~1806-1930	*CO bridge	*Nat. Commun.* 2022, 13, 3754 (Ref [42]) *Nat. Commun.* 2021, 12, 5745 (Ref [43])
1429	~1410	*COOH	*Angew. Chem. Int. Ed.* 2024, 63, e202412785 (Ref [44])
1367	~1380	*OCHO	*Angew. Chem. Int. Ed.* 2024, 63, e202410145(Ref [45])
1235	~1234	*CHO	*J. Am. Chem. Soc.* 2022, 144, 14936−14944 (Ref [46]) *Nat. Commun.* 2022, 13, 3754 (Ref [42])
1130, 1283	~1100, ~1340	*OC_2H_5	*Nat. Commun.* 2022, 13, 3754 (Ref [42])
1165	~1163, 1060	*COCHO	*J. Am. Chem. Soc.* 2022, 144, 14936−14944 (Ref [46])

References

1 Hung, S. F. *et al.* Identification of stabilizing high-valent active sites by operando high-energy resolution fluorescence-detected X-ray absorption spectroscopy for high-efficiency water oxidation. *J. Am. Chem. Soc.* **140**, 17263-17270 (2018).

2 Hung, S.-F. *et al.* In situ spatially coherent identification of phosphide-based catalysts: crystallographic latching for highly efficient overall water electrolysis. *ACS Energy Lett.* **4**, 2813-2820 (2019).

3 Wang, N. *et al.* Boride-derived oxygen-evolution catalysts. *Nat. Commun.* **12**, 6089 (2021).

4 Boker, S. *et al.* OpenMx: an open source extended structural equation modeling framework. *Psychometrika* **76**, 306-317 (2011).

5 Neale, M. C. *et al.* OpenMx 2.0: Extended structural equation and statistical modeling. *Psychometrika* **81**, 535-549 (2016).

6 Ozaki, T. Variationally optimized atomic orbitals for large-scale electronic structures. *Phys. Rev. B* **67**, 155108 (2003).

7 Ozaki, T. & Kino, H. Numerical atomic basis orbitals from H to Kr. *Phys. Rev. B* **69**, 195113 (2004).

8 Blöchl, P. E. Projector augmented-wave method. *Phys. Rev. B: Condens. Matter Mater. Phys.* **50**, 17953-17979 (1994).

9 Perdew, J. P. *et al.* Atoms, molecules, solids, and surfaces: Applications of the generalized gradient approximation for exchange and correlation. *Phys. Rev. B: Condens. Matter Mater. Phys.* **46**, 6671-6687 (1992).

10 Perdew, J. P. & Wang, Y. Accurate and simple analytic representation of the electron-gas correlation energy. *Phys. Rev. B: Condens. Matter. Mater. Phys.* **45**, 13244-13249 (1992).

11 Grimme, S., Antony, J., Ehrlich, S. & Krieg, H. A consistent and accurate ab initio parametrization of density functional dispersion correction (DFT-D) for the 94 elements H-Pu. *J. Chem. Phys.* **132**, 154104 (2010).

12 Tang, Y. *et al.* Adsorption behavior of Co anchored on graphene sheets toward NO, SO_2, NH_3, CO and HCN molecules. *Appl. Surf. Sci.* **342**, 191-199 (2015).

13 Peterson, A. A., Abild-Pedersen, F., Studt, F. & Rossmeisl, J. How copper catalyzes the

electroreduction of carbon dioxide into hydrocarbon fuels. *Energy Environ. Sci.* **3**, 1311-1315 (2010).

14 Peterson, A. A. & Nørskov, J. K. Activity descriptors for CO_2 electroreduction to methane on transition-metal catalysts. *J. Phys. Chem. Lett.* **3**, 251−258 (2012).

15 Nørskov, J. K., Rossmeisl, J., Logadottir, A. & Lindqvist, L. Origin of the overpotential for oxygen reduction at a fuel-cell cathode. *J. Phys. Chem. B* **108**, 17886-17892 (2004).

16 Somashekarappa, M. P., Keshavayya, J. & Sherigara, B. S. Synthesis and spectroscopic investigations of iron(III) complexes with chlorides and dianionic, symmetrically halogen substituted phthalocyanines as ligands. *Spectrochim. Acta A* **59**, 883-893 (2003).

17 KOBAYASRI, T. S., KUROKAWA, F., UYEDA, N. & SUITO, E. The metal-ligand vibrations in the infrared spectra of vluiofls metal phthalocyanines. *Spectroch. Acta A* **26**, 1305 -1311 (1970).

18 Martin, C. S., Gouveia-Caridade, C., Crespilho, F. N., Constantino, C. J. L. & Brett, C. M. A. Iron phthalocyanine electrodeposited films: characterization and influence on dopamine oxidation. *J. Phys. Chem. C* **120**, 15698-15706 (2016).

19 Lokesh, K. S. & Adriaens, A. Synthesis and characterization of tetra-substituted palladium phthalocyanine complexes. *Dyes Pigm.* **96**, 269-277 (2013).

20 Kumar, A. *et al.* Influence of substrate on molecular order for self-assembled adlayers of CoPc and FePc. *J. Raman Spec.* **49**, 1015-1022 (2018).

21 Li, X. *et al.* Identification of the electronic and structural dynamics of catalytic centers in single-Fe-atom material. *Chem* **6**, 3440-3454 (2020).

22 Liu, Z. *et al.* Switching CO_2 electroreduction toward ethanol by delocalization state-tuned bond cleavage. *J. Am. Chem. Soc.* **146**, 14260-14266 (2024).

23 Li, Y. C. *et al.* Binding site diversity promotes CO_2 electroreduction to ethanol. *J. Am. Chem. Soc.* **141**, 8584-8591 (2019).

24 Wang, T. *et al.* Ni-electrocatalytic CO_2 reduction toward ethanol. *Adv. Mater.* **36**, 2410125 (2024).

25 Hoang, T. T. H. *et al.* Nanoporous copper-silver alloys by additive-controlled electrodeposition for the selective electroreduction of CO_2 to ethylene and ethanol. *J. Am. Chem. Soc.* **140**, 5791-5797 (2018).

26 Wang, P. *et al.* Boosting electrocatalytic CO_2-to-ethanol production via asymmetric C-C coupling. *Nat. Commun.* **13**, 3754 (2022).

27 Ding, J. *et al.* A tin-based tandem electrocatalyst for CO_2 reduction to ethanol with 80% selectivity. *Nat. Energy* **8**, 1386-1394 (2023).

28 Herzog, A. *et al.* Operando investigation of Ag-decorated Cu_2O nanocube catalysts with enhanced CO_2 electroreduction toward liquid products. *Angew. Chem. Int. Ed. Engl.* **60**, 7426-7435 (2021).

29 Ma, G. *et al.* A hydrophobic Cu/Cu_2O sheet catalyst for selective electroreduction of CO to ethanol. *Nat. Commun.* **14**, 501 (2023).

30 Xia, W. *et al.* Adjacent copper single atoms promote C–C coupling in electrochemical CO_2 reduction for the efficient conversion of ethanol. *J. Am. Chem. Soc.* **145**, 17253-17264 (2023).

31 Xu, F. *et al.* Oxygen-bridged Cu binuclear sites for efficient electrocatalytic CO_2 reduction to ethanol at ultralow overpotential. *J. Am. Chem. Soc.* **146**, 9365-9374 (2024).

32 Li, J. *et al.* Weak CO binding sites induced by Cu-Ag interfaces promote CO electroreduction to multi-carbon liquid products. *Nat. Commun.* **14**, 698 (2023).

33 Qiao, Y. *et al.* Interfacial oxygen vacancy-copper pair sites on inverse CeO_2/Cu catalyst enable efficient CO_2 electroreduction to ethanol in acid. *Angew. Chem. Inter. Ed.* **64**, e202424248 (2025).

34 Luo, M. *et al.* Hydroxide promotes carbon dioxide electroreduction to ethanol on copper via tuning of adsorbed hydrogen. *Nat. Commun.* **10**, 5814 (2019).

35 Dutta, A. *et al.* Activation of bimetallic AgCu foam electrocatalysts for ethanol formation from CO_2 by selective Cu oxidation/reduction. *Nano Energy* **68**, 104331 (2020).

36 Chen, J. Y. *et al.* Operando analysis of NiFe and Fe oxyhydroxide electrocatalysts for water oxidation: detection of Fe^{4+} by mossbauer spectroscopy. *J. Am. Chem. Soc.* **137**, 15090-15093 (2015).

37 Li, J. *et al.* Identification of durable and non-durable FeNx sites in Fe–N–C materials for proton exchange membrane fuel cells. *Nat. Catal.* **4**, 10-19 (2021).

38 Wang, Q. *et al.* Attenuating metal-substrate conjugation in atomically dispersed nickel catalysts for electroreduction of CO_2 to CO. *Nat. Commun.* **13**, 6082 (2022).

39 Ding, L. *et al.* Over 70 % faradaic efficiency for CO_2 electroreduction to ethanol enabled by potassium dopant-tuned interaction between copper sites and intermediates. *Angew. Chem. Inter. Ed.* **61**, e202209268 (2022).

40 Zhu, S., Li, T., Cai, W.-B. & Shao, M. CO_2 electrochemical reduction as probed through infrared spectroscopy. *ACS Energy Lett.* **4**, 682-689 (2019).

41 Sultan, S. *et al.* Interface rich CuO/Al_2CuO_4 surface for selective ethylene production from electrochemical CO_2 conversion. *Energ Environ. Sci.* **15**, 2397-2409 (2022).

42 Wang, P. *et al.* Boosting electrocatalytic CO_2-to-ethanol production via asymmetric C–C coupling. *Nat. Commun.* **13**, 3754 (2022).

43 Zhang, G. *et al.* Efficient CO_2 electroreduction on facet-selective copper films with high conversion rate. *Nat. Commun.* **12**, 5745 (2021).

44 Ma, F. *et al.* Steering the site distance of atomic Cu−Cu pairs by first-shell halogen coordination boosts CO_2-to-C_2 selectivity. *Angew. Chem. Inter. Ed.* **63**, e202412785 (2024).

45 Yang, J. *et al.* Switching reaction pathways of CO_2 electroreduction by modulating cations in the electrochemical double layer. *Angew. Chem. Inter. Ed.* **63**, e202410145 (2024).

46 Zheng, M. *et al.* Electrocatalytic CO_2-to-C_{2+} with ampere-level current on heteroatom-engineered copper via tuning *CO intermediate coverage. *J. Am. Chem. Soc.* **144**, 14936-14944 (2022).